Alma Mater Studiorum · University of Bologna

School of Science
Department of Physics and Astronomy
Master Degree in Physics

Analysis of the clustering algorithm of the Micro Strip Detector in the FOOT experiment

Supervisor:
Prof. Matteo Franchini

Submitted by:
Riccardo Zini

Co-supervisor:
Dott. Gianluigi Silvestre

Academic Year 2022/2023

Where is everybody?
-Enrico Fermi

Abstract

Hadrontherapy is a medical treatment which employs high energy beams of charged particles to treat deep tumors in the body. The particular depth-dose profile is characterized by the release of the dose almost near the path end of the particle: the Bragg peak. This minimizes the damage to surrounding healthy tissue. However, nuclear interactions can occur between the particle beam and the human body generating beam fragments releasing dose beyond the Bragg peak and target fragments which release dose in healthy tissue. The lack of experimental cross section data is a problem in order to study the effects of these interactions. These effects are important also for radioprotection in space: long-term space missions are going to be planned in next years and risks on space radiation exposure for astronauts and electronics need to be studied. To fill these gaps in data, the FOOT (FragmentatiOn Of Target) experiment was proposed with the aim of measure double differential cross sections both in angle and kinetic energy with an uncertainty lower than 5%. In order to do that, it is composed by different subdetectors to detect, track and identify charged fragments produced in charged particle beam collisions with different targets.
In this thesis, one of the subdetector of FOOT is analyzed: the Micro Strip Detector (MSD). In particular, an analysis of the clustering algorithm is made to reduce the signal loss between readout strips: a first part dedicated to software changes and a second part focused on the application of the η correction. The analysis is performed with data from GSI 2021 campaign of ^{16}O at 400 MeV/u and from CNAO 2022 campaign of ^{12}C at 200-300 MeV/u.

Contents

Introduction

Handrontherapy is an innovative radiation therapy technique to treat solid tumors using protons and heavier ions. The main advantage is the different behaviour of charged particles respect to photons used in radiotherapy: the depth-dose profile is characterized by an energy release mostly near the end of the particle path, forming the Bragg Peak. This helps in therapy in order to release most part of the radiation in the tumor region, reducing issues to healthy tissues and organs. While in conventional radiotherapy, X-rays radiation intensity has a maximum and then decrease exponentially in the material.

However, hadrontherapy involves nuclear interaction which can induce fragmentation on beam particles, the produced fragments have high energy and release dose in the body beyond the Bragg Peak. Moreover, fragmentation involves also human body nuclei producing target fragments with lower energy, which have short ranges, releasing dose in healthy tissue. Both fragments type effects need to be studied in detail given the lack of cross section data.
The study of nuclear fragmentation is fundamental also for space radioprotection, therefore in these years long-term space mission outside Earth's orbit became important for space agencies like NASA. In this case, space and cosmic radiations are the main sources of fragmentation processes which can have strong effects on astronauts health prevention and on electronics protection.

The FOOT (FragmentatiOn Of Target) experiment aims to fill this lack of data by measuring the cross sections both for target and projectile fragmentation. To obtain this result, the experiment adopts an inverse kinematic approach for the measurement of target fragments to deal with their problems of short range.

The aim of this thesis is the improvement of the clustering algorithm for the Micro Strip Detector (MSD). Two main improvements are applied to the double threshold algorithm in order to correctly define η, a parameter which represents the center of gravity of the two highest readout strips in the cluster. The first improvement involves the number of strip in clusters: two strips are added at every cluster extremes. Then also noisy strips are considered and handled in cluster composition in order to take into account their impact in cluster formation.
The following step of the analysis was the application of a correction on cluster signals

depending on the η. These implementations are analyzed using data from two different campaigns: ^{16}O at 400 MeV/u from GSI 2021 and ^{12}C at 200-300 MeV/u from CNAO 2022.

In Chapter 1 charged particles behaviour for electromagnetic and nuclear interactions with matter are presented. In Chapter 2, the hadrontherapy and space protection are reported with a brief focus on the main aspects of radiobiology effects. In Chapter 3, the FOOT experiment goal and characteristics of each subdetector are introduced. In Chapter 4, the analysis on the MSD is described presenting the algorithm changes and corrections. In Chapter 5, the results of the implementation are reported and discussed.

Chapter 1

Charged particle interactions

In order to describe hadrontherapy, an overview of charged particles interactions is required; they can undergo mainly electromagnetic or nuclear interaction in the hadrontherapy energy ranges. In this chapter main aspects of both are presented.

1.1 Electromagnetic interaction

The two main electromagnetic processes which can occur for a charged particle passing through a material are: an inelastic scattering with atomic electrons which is the main way to loose energy and an elastic scattering with nuclei deviating particle from initial direction. They are described in the following sections.

1.1.1 Interaction with atomic electrons: Bethe-Bloch formula

Ionization is the main energy loss process occurring when a charged particle traverses a medium. It is an electromagnetic interaction, characterized by elastic collisions of particles with electrons considered at rest and assuming that particle mass is really greater than electron mass ($M >> m_e$), i.e. considering heavy charged particles not being deviated while traversing the material. The mean energy loss for unit length of a particle, expressed in MeV/cm, is given by the Bethe-Bloch formula:

$$-\left\langle \frac{dE}{dx} \right\rangle = 4\pi N_A r_e^2 m_e c^2 \frac{z^2}{\beta^2} \frac{Z}{A} \left[ln \frac{2m_e c^2 \beta^2 \gamma^2 T_{max}}{I^2} - \beta^2 - \frac{\delta(\beta\gamma)}{2} - \frac{C}{Z} \right] \cdot \rho \qquad (1.1)$$

where there are constants (N_A is the Avogadro number, r_e classical radius of the electron and m_e its mass, c is the speed of light in vacuum), incident particle properties (charge z and velocity β) and material ones (density ρ, proton to neutron ratio Z/A, mean excitation energy I) and the correction factors: δ and C.

Usually the energy loss is expressed as the stopping power:

$$S = -\frac{dE}{dx} \tag{1.2}$$

In 1.1 there is a density dependence, however the dE/dx can be divided for the density obtaining the energy loss as a function of mass thickness, which can be measured in MeV$\cdot$ cm^2/g. In this way the radiation has the same effects on a given unit of mass thickness independently from the different medium material density. An important feature of the stopping power is its small dependence on the traversed material represented in the Z/A ratio: for light nuclei this factor is $\sim 1/2$, while for heavier nuclei it is slightly smaller because of the predominance of neutrons over protons, thus energy loss becomes slower for larger Z.

Behaviour and corrections

As it is represented in Fig. 1.1, at low β the stopping power has a $1/\beta^2$ dependence dominates until a point called MIP (Minimum Ionizing Particle) where the logarithmic rise begins, after that the relativistic correction lowers the shape of the function; therefore for a relativistic particle at high velocities the transverse electric field goes from E to γE, more atoms interacting with incoming particle yielding a larger energy loss.
An effect present at high energies is the density correction δ: a charged particle has a polarization effect on atoms of the traversed material due to the presence of the electric field. Polarized atoms act as a shield for furthest atoms, reducing the long range interaction of particles. For large $\beta\gamma$ the polarization effect is stronger, because un-polarization takes more time.
At low energies, instead, there is the shell correction: when the velocity of the particle is almost equal to the orbital velocity of electrons, the electron can't be considered at rest anymore and there can be capture effects.
The hadrontherapy energy range is in the region mainly dependent on $1/\beta^2$, which means that the slower is the particle, the higher is the energy released until it stops and the higher is the charge, the more is the energy release in unit of length, as explained in Sec. 2.1.1.

1.1.2 Energy straggling

The energy loss expressed in 1.1 is reported as a mean quantity because the interaction it is a stochastic process, for the same path of the same particle at a fixed momentum different values are obtained for repeated measurements due to statistical fluctuations:

$$\Delta E = \sum_{n=1}^{N} \delta E_n \tag{1.3}$$

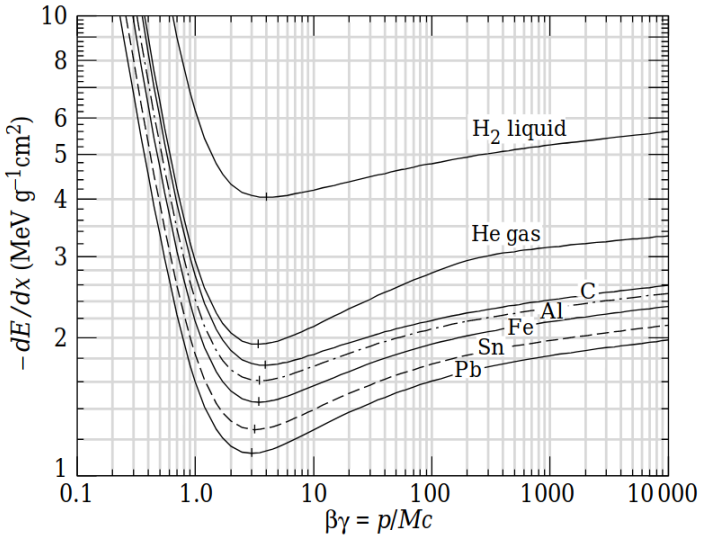

Figure 1.1: Stopping power in function of $\beta\gamma$ for z=1 particles in different materials [1].

therefore the total energy loss ΔE is the sum of infinitesimal energy losses δE in each one of the N collisions. These fluctuations cause the energy loss straggling. In left side of Fig. 1.2 it is shown that there is no energy transfer under a certain value called excitation threshold and the probability is higher for smaller energy losses, corresponding to distant collisions. It is important to notice that collisions with big energy losses (small impact parameter) are unlikely but not impossible. In right side of Fig. 1.2 there are different probability distributions (Gaussian with an high energies tail) for different absorber thickness, it is evident that the asymmetry is more evident for thinner absorbers while for thicker there is a more symmetric distribution. In the limit of many collisions, the probability distribution can be described as:

$$f(\Delta E) = \frac{1}{\sqrt{2\pi\sigma}} exp \frac{(\Delta E - \overline{\Delta E})^2}{2\sigma^2} \tag{1.4}$$

which is a Gaussian distribution as a consequence of the central limit theorem.

1.1.3 Range of a particle

An important quantity is the range defined as the distance covered by the particle until loses all its energy:

$$R = \int_0^{E_0} \left(\frac{dE}{dx}\right)^{-1} dE, \tag{1.5}$$

where E_0 is the initial particle energy. Given the energy dependence of the range, also its measurement is influenced by fluctuations (left side Fig. 1.3) giving rise to range

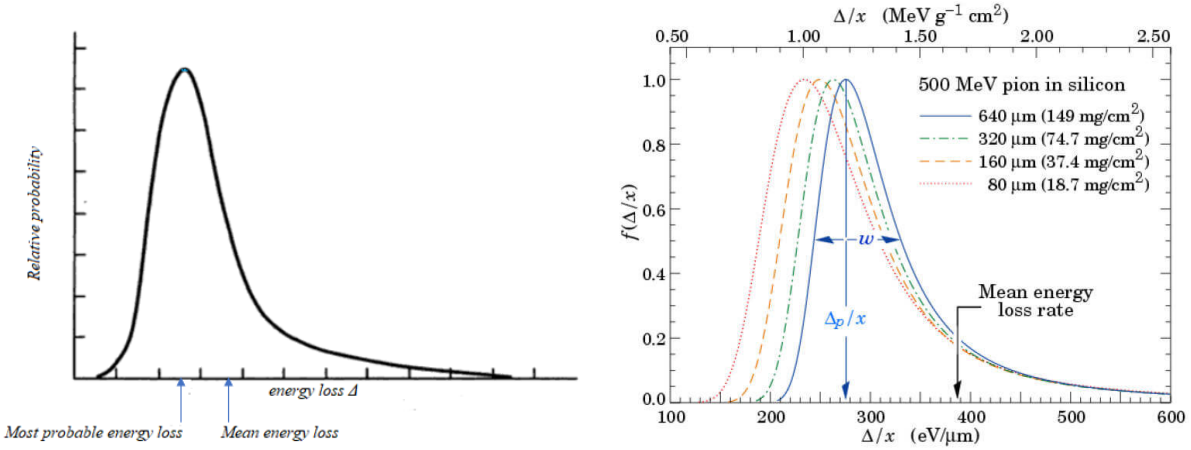

Figure 1.2: Probability of transferring energy in function of the energy loss itself: threshold at low energies, then the maximum and the final tail (left). Energy straggling function for different material thickness for a 500 MeV pion in silicon (right) [2].

straggling σ_r whose relative value can be written as [3]:

$$\frac{\sigma_R}{R} = \frac{1}{\sqrt{m}} f\left(\frac{E}{mc^2}\right) \tag{1.6}$$

The increasing behaviour of range straggling respect to the range is represented in right side of Fig. 1.3. This aspect is fundamental in hadrontherapy as explained in Sec. 2.1.3.

1.1.4 Interaction with nuclei

Depending on the energy and impact parameter, an incoming particle can interact also with nuclei Coulomb field through elastic collisions, the main effect is deviating particle from initial direction. Scattering angles distribution is described by the Molière's theory [5] in which standard deviation σ_θ can be described as:

$$\sigma_\theta = \frac{13.6\,\text{MeV}}{\beta cp} z \sqrt{\frac{x}{X_0}} \left[1 + 0.038\ ln\left(\frac{x}{X_0}\right)\right] \tag{1.7}$$

where β, p and z are particle velocity, momentum and charge while x and X_0 are material thickness and radiation length.
This deviation leads to a lateral displacement by Coulomb scattering to be considered in hadrontherapy (2.1.3).

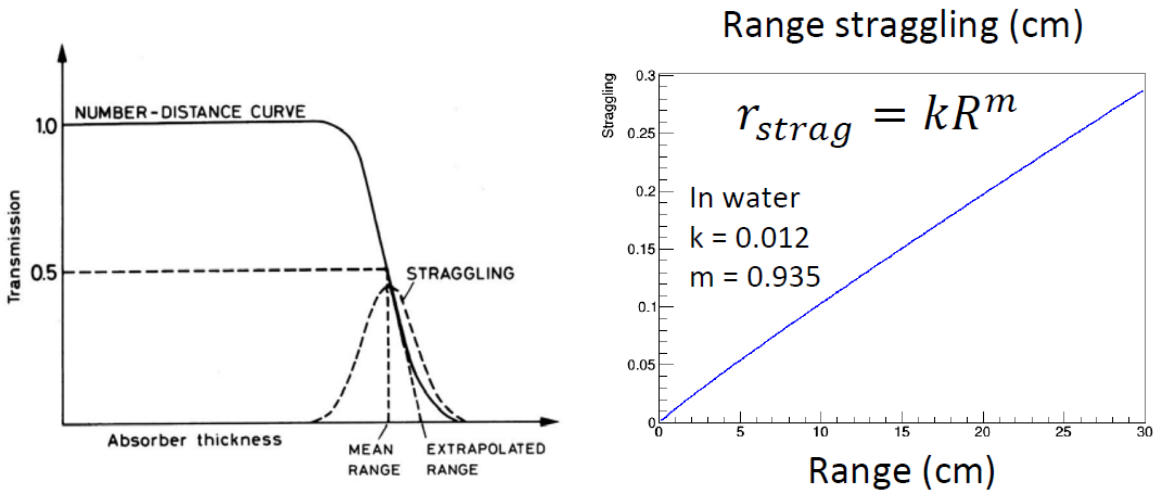

Figure 1.3: Transmission coefficient in function of the range, mean range and straggling (left). Range straggling behaviour with respect to particle range (right) [4].

1.2 Nuclear Interaction

Up to now only the electromagnetic interaction was considered, but in order to fully describe hadrontherapy processes and to analyze charged particles behaviour in matter nuclear interaction has to be also considered.
A general nuclear reaction can be considered as the interaction between two nuclei: the projectile and the target. It can be divided in elastic, where there is only a re-distribution of the energy, and inelastic where new nuclear species are produced. At hadrontherapy energies the most frequent reaction is fragmentation: an inelastic peripheral collision in which few nucleons participate. This process is described by the abrasion-ablation model represented in Fig. 1.4: after the collision there is the abrasion phase where target and projectile are fragmented forming a fireball, an excited state of nucleons. Then, in the ablation phase, nuclei de-excite emitting light and massive fragments. These nuclei fragments have non negligible impact in hadrontherapy processes.

1.2.1 Target and projectile fragmentation

Nuclear interaction can induce fragmentation both in projectile and target depending on nuclear species involved in the interaction. For a proton-proton collision there can't be fragmentation; for a proton colliding on target formed of heavier nuclei there is target there is target fragmentation while the inverse process gives projectile fragmentation. An interaction between nuclei both heavier than protons induce fragmentation in both nuclei. In the projectile fragmentation, the produced fragments have an energy similar to the projectile so they're easier to detect and to obtain experimental data and results.

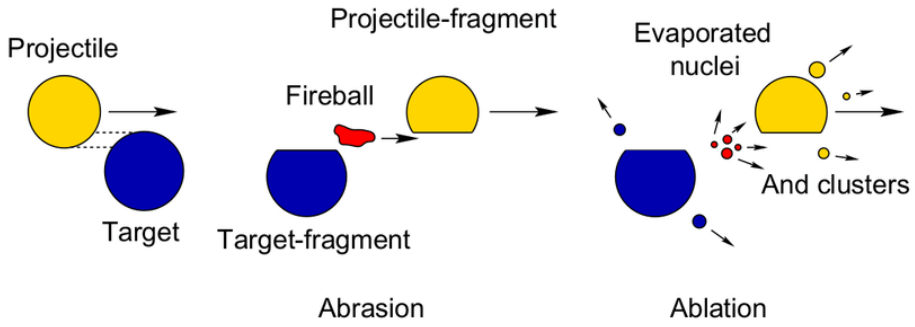

Figure 1.4: Nuclear fragmentation scheme: interaction between projectile and target, fireball formation (abrasion) and final reaction products (ablation) [6].

The problem raises with target fragmentation: the target is at rest therefore fragments have very low energy travelling really short distances (few μm) making them virtually impossible to be measured. This difference is highlighted in section 2.4 where experimental data for hadrontherapy of both cases are presented showing also the adopted approach to solve this problem by the FOOT collaboration.

1.2.2 Nuclear cross section

The cross section measures the probability of a given interaction to take place. Considering a detector placed to record particle emitted in a direction θ with respect to the beam, the detector defines a small solid angle $d\Omega$ with respect to the target (Fig. 1.5). The beam a has a number of particles per unit time I_a while N is the target nuclei per unit area and R_b the outgoing particles rate, the reaction cross section is obtained as:

$$\sigma = \frac{R_b}{I_a N} \tag{1.8}$$

which defined in this way has the dimension of area per nucleus. However, in many nuclear physics applications the key parameter is the probability to find a particle emitted at a certain angle with a certain energy, therefore the definition of cross section must be modified considering $d\Omega$ and dE. This gives the so-called double differential cross section $d^2\sigma/dE_b d\Omega$ [7] which integrated provides the total cross section of a given reaction:

$$\sigma = \int_0^{\Omega} \int_0^{E} \frac{d^2\Omega}{d\Omega dE} d\Omega dE \tag{1.9}$$

In general the nuclear cross section can also be expressed as:

$$\sigma_r = \pi(R + \lambda)^2 \tag{1.10}$$

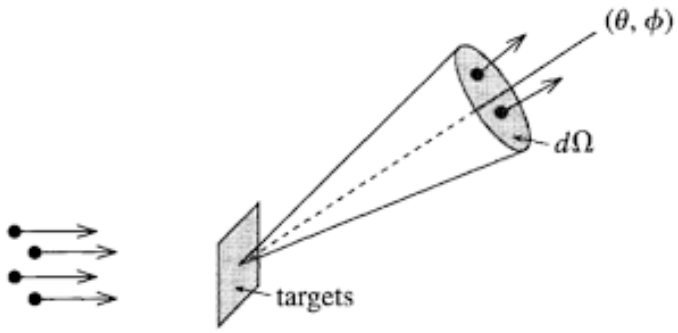

Figure 1.5: Reaction geometry showing incident beam, target, outgoing beam and solid angle $d\Omega$.

where R and λ are the target and projectile transverse dimension.
In order to describe the cross section behaviour for different targets it is used the semiempirical model described by Bradt-Peters law that it is valid for proton with $E \geq 15\,\mathrm{MeV}$ and nuclei with $E \geq 100\,\mathrm{MeV/u}$:

$$\sigma_r = \pi r_0^2 c_1 \left(A_p^{1/3} + A_t^{1/3} - b_0\right)^2 \tag{1.11}$$

where r_0 is the nuclear radius ($\approx 1.25\,\mathrm{fm}$), A_p and A_t are mass number of projectile and target respectively, b_0 and c_1 are parameters.

Chapter 2

Hadrontherapy and Space protection

Charged particles behaviour has an important impact on biological tissues which effects can be studied mainly for two application: the hadrontherapy and the radio-protection in space. The first concerns charged particle interactions with cancer cells in order to treat a patient, the second one studies astronauts consequences due to radiation exposure in space. Their main aspects are presented in this chapter.

2.1 Hadrontherapy

Hadrontherapy is a cancer treatment consisting in the release of radiation energy through charged ions. The main goal is to maximize the damage on cancer cells and minimize the effect on healthy cells. Cancer is a large group of diseases that can start in almost any organ or tissue of the body when abnormal cells grow uncontrollably [8]. So far the causes of cancers are not well known, but there are therapies to treat some of them: surgery, chemotherapy, immunotherapy, radiotherapy and hadrontherapy (which is the focus of this thesis). Focusing on the last two of them, they both consist on irradiation of the cancer region to destroy tumor cells preventing their reproduction. The difference between them is that radiotherapy adopts electromagnetic radiation (photons or electrons) while hadrontherapy uses hadrons (proton, neutrons and ions) to radiate the tumor region.
The first idea of hadrontherapy was given in 1945 by Robert Wilson, one of the founder of Fermilab, who proposed to use hadrons for radiotherapy and few years later in 1954 at Lawrence Berkeley National Laboratory (California) the first patient was treated with this technique. From that moment the research and treatments with protons, neutrons and charged particles began. There are hundreds hadrontherapy centers in the world [9], three working in Italy: CNAO (Centro Nazionale di Adroterapia Oncologica) [10] located in Pavia providing beam of protons and ^{12}C ions taken by a synchrotron, Centro di Protonterapia in Trento [11] which exploits proton beams using a cyclotron

and CATANA (Centro di AdroTerapia ed Applicazioni Nucleari Avanzate), in Catania, where eye tumors are studied [12].
Today proton and ^{12}C ions are mainly used to treat solid tumors, but other particles such as neutrons, He and other light ions nuclei (like Li, O, up to Si ions) have been either used or studied to be used for the future clinical treatments.
The main goal of hadrontherapy consists in treating the tumor preventing its indefinite proliferation damaging its DNA, so that the cancer cell would lose the capability to reproduce itself and con be considered dead. The main collateral effect, as in conventional radiotherapy, is the release of radiation also on healthy tissue, aspect which is crucial for every treatment.

2.1.1 Bragg Peak

Since collateral effects (1.1.3, 1.1.4) are present it is fundamental to describe charged particle interactions as accurate as possible, in order to limit the risk factor of the treatment; therefore the biological effects occurring in human body due to radiation have to be considered. A more detailed radiobiological description is reported in Section 2.2. To describe them it is important to define the following quantities.
The fluence is defined as the number of particles per unit of area perpendicular to the beam: $\Phi = dN/dA$, expressed in number of particles over cm^2. The quantity used as reference in treatments is the *Dose* which is defined as the absorbed energy per unit mass:

$$D = \frac{dE}{dm} = \Phi \frac{dE/dx}{\rho}, \tag{2.1}$$

it is measured in Gray (1 Gy= 1 J/Kg) and can be expressed in terms of the stopping power, particle fluence and density (ρ) of the traversed material.
The key element in hadrontherapy is the peculiar shape of the released dose in terms of the particle range, reported in Fig. 2.1. The dose profile for charged particles (proton and carbon in the plot) is related to 1.1: the curve is almost constant in the entrance channel where kinetic energy is high and $dE/dx \propto ln(E)$. When the kinetic energy starts to decrease the energy loss is $\propto 1/\beta^2$ leading to an increase of the energy release up to a very clear peak, the Bragg Peak, after which the particle stops. In the plot the difference between a charged particle and a photon is highlighted. The proton has a completely different behaviour: an initial growth followed by a maximum and a slow constant decrease. This lead to the main advantage of hadrontherapy respect to radiotherapy, namely a release of the most part of the energy when the particle is about to stop. A photon, instead, release energy with a small decrease during its path in the material. This reflects to treatment is behaviour where the radiation is released mostly in one region (hadrontherapy) or in the all track (radiotherapy). The range depends on initial energy of a charged particle (1.1.3), as a consequence in hadrontherapy treatment the Bragg Peak position, so the range, can be chosen just managing the initial energy.

Once the tumor location is known, it is possible to have the Bragg Peak in that region. In this way the most part of the dose is released in tumor region reducing, respect to radiotherapy, the dose released in surrounding healthy tissue.

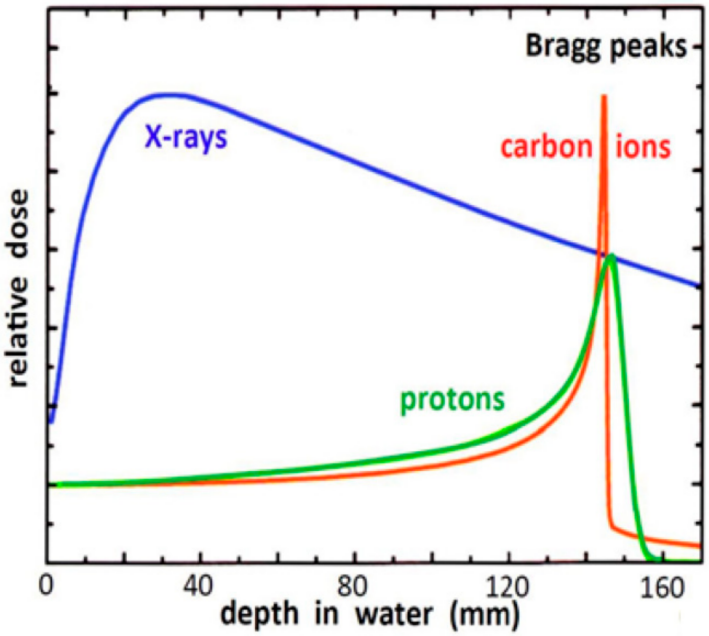

Figure 2.1: Dose released by X-rays (in blue), protons (green) and carbon (red) in function of the depth in water [13].

2.1.2 Spread Out Bragg Peak

The Bragg Peak has an average width of few millimetres, smaller than typical tumor size which is of the order of centimeters. To overcome this problem the beam energy is slightly changed in order to obtain a release of radiation in the full depth of the tumor itself. In this way the so called Spread Out Bragg Peak (SOBP) is obtained, represented in Fig. 2.2.
The shape of the SOBP depends on particle beam type and on cancer depth: for a larger depth more peaks are needed leading to more energy released before the cancer causing issues to healthy tissue. In order to obtain a SOBP, according to the provided accelerator, it is possible to apply a degrader on a fixed energy beam, which is spread on energy and no more monochromatic (with cyclotrons), or just accelerating articles with different energies, obtaining in this way a pulse flux (with synchrotrons) [14].

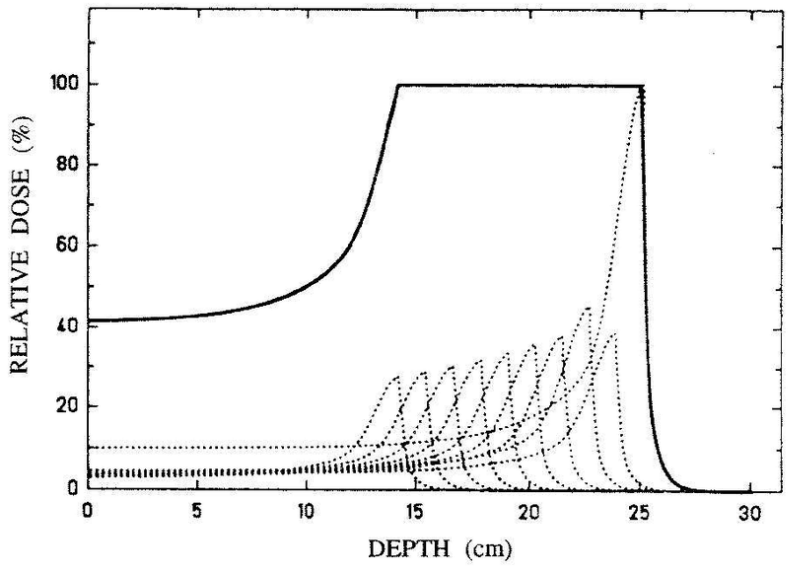

Figure 2.2: Spread Out Bragg Peak representation: the overall dose released (continuous line) is the sum of all single peaks (dashed lines) [15].

2.1.3 Hadrontherapy effects

Radiotherapy and hadrontherapy have different different release of energy in the body which is the main advantage in the use of charged particle respect to photons, however there are collateral effects in hadrontherapy to consider: straggling and nuclear fragmentation.
In previous chapter were already mentioned two effects of charged particle interaction: the longitudinal displacement due to the statistical behaviour of the energy release (1.1.3) and the lateral displacement given by the interaction with nuclei field (1.1.4). Another contribution is the fragmentation due to nuclear interaction of particles: considering two different ions like proton and Carbon (Fig. 2.1) is recognizable in both cases the Bragg Peak, however in Carbon case there is an evident tail after the peak. That is caused by the projectile fragmentation in heavy ion interaction, the produced fragments travel longer distances respect to Carbon giving rise to the tail after the peak. In this way the radiation affects also healthy tissue above the peak.
Both straggling and nuclear fragmentation reflect an undesirable release of energy which has to be considered in hadrontherapy.

2.2 Radiobiology

The goal of hadrontherapy is stop reproduction and proliferation of cancer cells inducing damages using charged ions.
The damage to the DNA could be induced by two different processes: *direct* or *indirect*, both sketched in left side of Fig. 2.3. In the *direct* way the radiation hits the DNA breaking the chemical bonds in two different types of damages (right side Fig. 2.3): a single strand break and a double strand break. The first one is reparable as the damaged part of the strand is recovered by "copying" the correct sequential from the other strand. The second is not possible to repair if the damage is in the same region of both strands. In the *indirect* way the radiation doesn't involve directly the DNA: the damage is produced by free radicals (OH) that are formed by ionization in the hydrolysis of the water present in the cell.

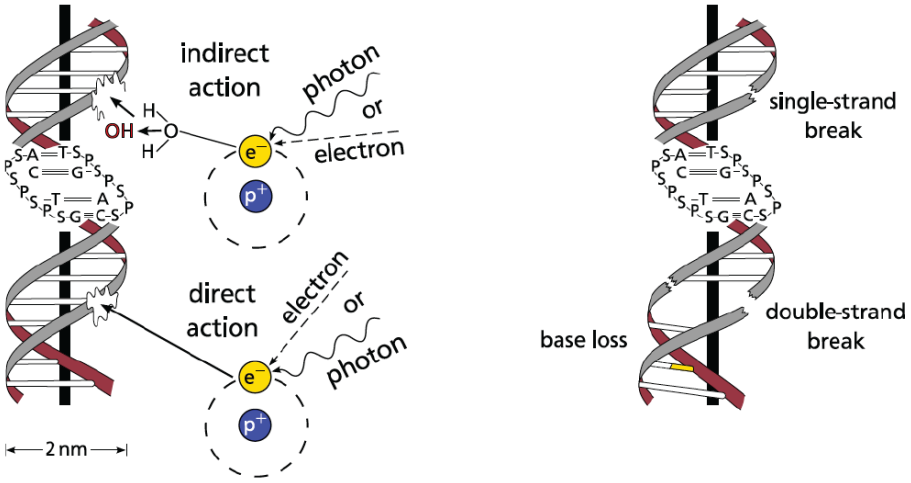

Figure 2.3: Damages on DNA strand: direct and indirect radiation effects of free radicals (left) and representation of single and double strand break (right) [16].

2.2.1 Linear Energy Transfer

In radiobiology an important quantity used to categorize radiation damage is the *Linear Energy Transfer* (LET), defined as the energy transferred per unit distance from the ionizing particle to the material:

$$LET = \frac{dE}{dl} \tag{2.2}$$

expressed in KeV/μm. The LET indicates the energy focused on the particle, excluding secondary electrons with high energy. While stopping power defined in 1.1 refers to the

Radiation	LET (keV μm^{-1})
1 MeV γ rays	0.5
20 keV β^- particles	10
5 MeV α particles	50

Table 2.1: Approximate values of LET for different types of radiation [17].

energy released in the material, therefore they equalize if high energies electrons are considered. From this definition, it follows that radiations which are easily stopped will have a high LET, those which are penetrating will have a low LET. Some example values are given in Table 2.1.

2.2.2 Linear Quadratic model

In order to describe the biological effect of radiation, which strongly depends on the released dose, the Linear Quadratic Model has been defined: it is based on Poisson Statistics of cell deaths due to randomly distribution of the ionizations produced by the radiation. It also considers the difference between single and double strand break, defining the *survival probability*:

$$S(D) = \exp\left(-\alpha D - \beta D^2\right) \tag{2.3}$$

where α and β are two constants depending on the radiation type and D is the dose. In detail, α describes the not repairing damages and β refers to repairing damages. In Fig. 2.4 is reported the survival fraction referred to α and β contributions. The ratio α/β is the dose value for which the linear and quadratic components are equal. It can assume different values according to the type of tissue considered: for resistant tissue to radiation $0.5 < \alpha/\beta < 6$ Gy while for less resistant tissue $7 < \alpha/\beta < 20$ Gy. Experimental data agree with Linear Quadratic Model over a wide range of dose and tissues. However, it does not take into account treatment time and dose rate. More details about radiobiology in ions therapy can be found in [18].

2.3 Radioprotection in Space

The measurements performed with the FOOT experiment could be also interesting for other applications, like radioprotection in space. NASA and other space agencies have started since several years the risk evaluation for astronauts in view of long duration space missions, such for instance the travel to Mars [20]. Several radiation sources have to be considered, then the design and optimization of the spacecraft shielding requires a detailed knowledge of fragmentation processes.

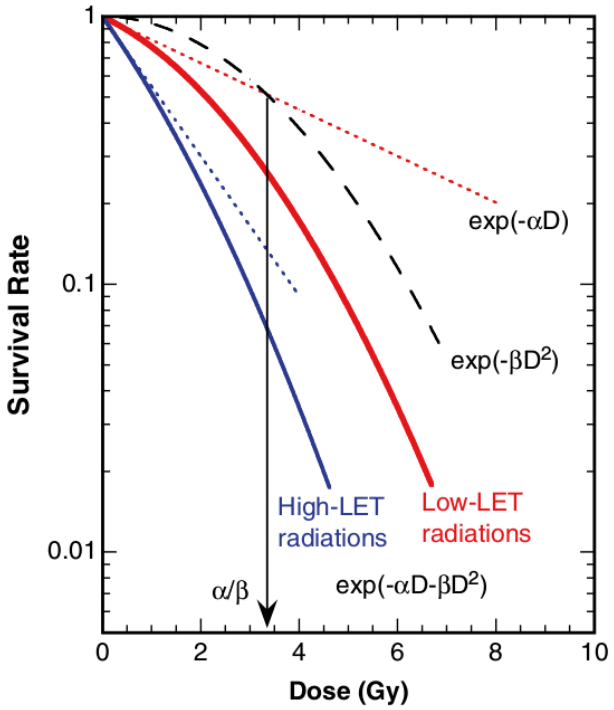

Figure 2.4: Survival curves related to α and β parameters in the Linear Quadratic model. Overall cell survival curves (solid lines) for low and high-LET radiations are plotted with each component in the LQ equations as the linear components (dotted lines) and quadratic components (broken line). The black arrow indicates the α/β value [19].

There are three main sources of energetic particles in space: Solar Particle Events (SPEs), Galactic Cosmic Rays (GCR) and the geomagnetically trapped particles.

Solar Particle Events

The sun releases electromagnetic radiation and also a flux of particles, the solar wind, mainly composed of protons and electrons of energy between 1.5 and 10 KeV. These particles are accelerated during solar flares up to the GeV region, these energy can inflict a lethal dose to astronauts.

Galactic Cosmic Rays

Galactic Cosmic Rays (GCRs) consist of high energy protons and charged particles originated from supernovae, their energy spectrum ranges from MeV to TeV (Fig. 2.5). The elemental abundance and energy spectrum of the Galactic Cosmic Rays are well known: 86% of protons, 12% of alpha particles, 1% of heavier ions like Carbon, Silicium

and Iron. However, their biological effects are poorly understood. Even if heavy ions are rare with respect to protons and alphas, they contribute significantly to the total dose because of its dependence from the square of the nuclear charge described by 1.1. Moreover, the GCR radiation cannot be easily shielded because of the nuclear fragmentation into lighter and thus more penetrating ions.

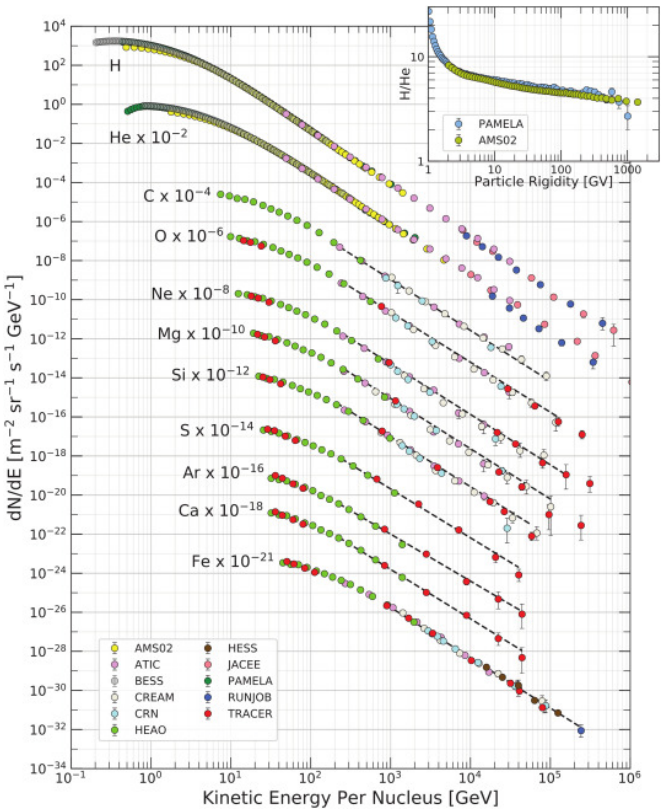

Figure 2.5: Cosmic ray flux for different species [21].

Geomagnetically trapped particles

The geomagnetically trapped particles consist of protons and electrons confined by the Earth magnetic field in two regions, called Van Allen belts. Protons reach energies up to a few hundreds MeV in the inner belt and electron up to 100 KeV in the outer belt [22]. These belts can be crossed quickly by deep space mission spacecrafts, so risks concern mainly human missions or satellites in Low Earth Orbit (LEO).

2.3.1 Analogies with hadrontherapy

There is a common ground between protecting astronauts from the harmful effects of space radiation and providing tumor therapy to patients using ions. The particle species currently available in hadrontherapy (protons and Carbon) or considered as promising alternative candidates (Helium, Lithium and Oxygen) are among the most abundant in space. The overlap is also in terms of energy, especially around the optimum for tumor therapy. This is the same energy region of the solar flare protons and Van Allen trapped protons as well as near the peak of the GCR spectrum. The shared interest of ion species and energy range between space radioprotection and hadrontherapy allows the interchange of cross sections data as presented in Sec. 2.4.
Recent studies [23][24][25] on nucleus-nucleus reaction cross section in space show a lack of data in the energy range of interest for both hadrontherapy and space radioprotection with an evident discrepancy between real data and models. Cross sections are partial (differential in angle or in kinetic energy) and only with reference to the initial energy of the beam, instead of the fragment energy itself. To overcome the described issues, the current results are not enough and new measurements are needed.

2.3.2 Shielding

Cross sections for nucleus–nucleus interactions that produce a charge change in the projectile are accurately described by Bradt and Peters (Eq.1.11). Wilson and Townsend presented a slightly modified version for use in NASA space radiation transport codes [26]:

$$\sigma_{cc} = \pi r_0^2 \left(A_p^{1/3} + A_t^{1/3} - 0.2 - 1/A_p - 1/A_t \right)^2 \tag{2.4}$$

where σ_{cc} is the charge-changing cross section and other quantities are the same used in Brad-Peters law.
Shielding goal is to reduce the risk from heavy ions due to the effects of nuclear fragmentation. Although heavy ions ($Z > 2$) represent only about 1% of the GCR flux, their contribution in unshielded space can be from 30% to 40% of the total dose . In particular, Iron ($Z = 26$) in free space make the largest contribution of any single ion species, despite being less abundant than protons by nearly four orders of magnitude.
Currently, spacecrafts have been constructed with aluminum hulls. Given the knowledge of the fragmentation cross sections of many ion species at typical GCR energies, can be estimated the fluxes attenuation for various primary ions by fragmentation passing through a hull. Table 2.2 shows the results for several important species using cross sections calculated with 2.4. Note that for the lighter ions are expected some replenishment by fragmentation of heavier ions ($Fe + Al \rightarrow Si + X$, etc). It is notable that $20\,\mathrm{g/cm^2}$ of aluminum is sufficient to break up the majority of incident iron ions and roughly half of magnesium and silicon ions.

Ion	5 g/cm^2 Al	10 g/cm^2 Al	20 g/cm^2 Al	40 g/cm^2 Al
^{12}C	0.128	0.240	0.423	0.667
^{16}O	0.141	0.261	0.455	0.702
^{24}Mg	0.160	0.295	0.503	0.753
^{26}Si	0.169	0.309	0.522	0.772
^{56}Fe	0.213	0.381	0.617	0.853

Table 2.2: Calculated attenuation of high-energy ions by fragmentation in aluminum (Al) using geometric cross sections [27].

2.4 Experimental Data

2.4.1 Cross section for hadrontherapy

In the following the currently existing experimental data on fragmentation cross section will be discussed keeping in mind both the hadronic cross section behaviour and the semi empirical model presented in section 1.2.
In Fig. 2.6 there is the model to data comparison of the reaction cross section for target fragmentation of a proton colliding to a Carbon and Oxygen target. The reference kinematic variable is the kinetic energy of the projectile (the proton). In this case, the main problem rises in the cross section for the different fragments produced in that reaction (Fig. 2.7) because few experimental points are present. In the figure, it is clear the lack of data in the range of interest for hadrontherapy. The only cases in which the energy range is sufficiently covered is for the production of ^7Be and ^{11}C because they have been studied as important isotopes for PET diagnostic technique. Moreover, it would be instead more useful to measure the cross section of each produced fragments with respect to its energy and not to the beam energy. This measure is fundamental because produced fragments have different charge with respect to the initial beam, leading to different energy release in the material and different range. The current results obtained are not enough and new measurement are needed. This is the main goal of the FOOT experiment.
In Fig. 2.8 cross sections for projectile fragmentation are reported. For Carbon (^{12}C) beam into Hydrogen, Carbon and Oxygen targets. In this case, as expected for projectile fragmentation (1.2.1), there are many experimental points due to the easier way to detect fragments.

2.4.2 Inverse kinematics approach

As suggested in Section 1.2.1, in order to measure target fragmentation cross sections the inverse kinematics approach is used. Instead of considering a proton beam colliding

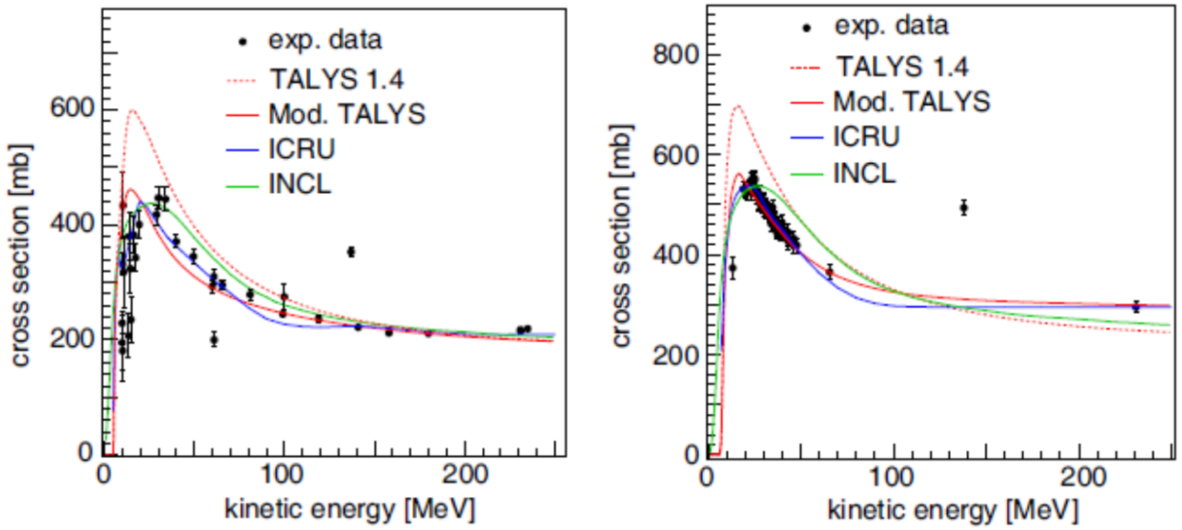

Figure 2.6: Cross section comparison between different models and experimental data for $p + ^{12}C \rightarrow X$ (left) and $p + ^{16}O \rightarrow X$ (right) [28].

on a Carbon target, it is possible to consider a Carbon beam colliding on a proton target and applying a Lorentz transformation to move the reference frame from the fixed target reference frame to the projectile one (as schematized in Fig. 2.9). In this way the produced fragments have enough energy to be detected and an inverse Lorentz transformation gets back the required kinematic quantities to the desired reference frame. A schematic example of the process will be shown.
Considering a generic four-vector $\mathbf{A}$ in the laboratory frame:

$$\mathbf{A} = (a_t, \vec{a})$$

where a_t and $\vec{a}$ are the temporal and spatial vector component, the Lorentz transformation is written as:

$$\mathbf{A}' = \Lambda \mathbf{A}$$

where $\mathbf{A}'$ is the four-vector in the projectile frame and Λ is the 4×4 transformation matrix. In the case considered the transformation happens only in the x direction therefore can be expressed as:

$$\begin{pmatrix} a'_t \\ a'_x \\ a'_y \\ a'_z \end{pmatrix} = \begin{pmatrix} \gamma & 0 & 0 & -\beta\gamma \\ 0 & 1 & 0 & 0 \\ 0 & 0 & 1 & 0 \\ -\beta\gamma & 0 & 0 & \gamma \end{pmatrix} \cdot \begin{pmatrix} a_t \\ a_x \\ a_y \\ a_z \end{pmatrix} = \begin{pmatrix} \gamma a_t - \beta\gamma a_z \\ a_x \\ a_y \\ -\beta\gamma a_t + \gamma a_z \end{pmatrix}$$

where β is the velocity and $\gamma = 1/\sqrt{1-\beta^2}$ is the relativistic factor, this gives rise to the inverse transformation:

$$\begin{pmatrix} a_t \\ a_x \\ a_y \\ a_z \end{pmatrix} = \begin{pmatrix} \gamma & 0 & 0 & \beta\gamma \\ 0 & 1 & 0 & 0 \\ 0 & 0 & 1 & 0 \\ \beta\gamma & 0 & 0 & \gamma \end{pmatrix} \cdot \begin{pmatrix} a'_t \\ a'_x \\ a'_y \\ a'_z \end{pmatrix} = \begin{pmatrix} \gamma a_t - \beta\gamma a_z \\ a_x \\ a_y \\ -\beta\gamma a_t + \gamma a_z \end{pmatrix}$$

Using the space $\mathbf{S} = (ct, x, y, z)$ and momentum $\mathbf{P} = (E/c, p_x, p_y, p_z)$ vectors the kinematic quantities needed are obtained, in this way cross sections can be computed. This method is adopted by FOOT experiment (Section 3.1) to obtain cross sections measurements in order to have a more complete dataset.

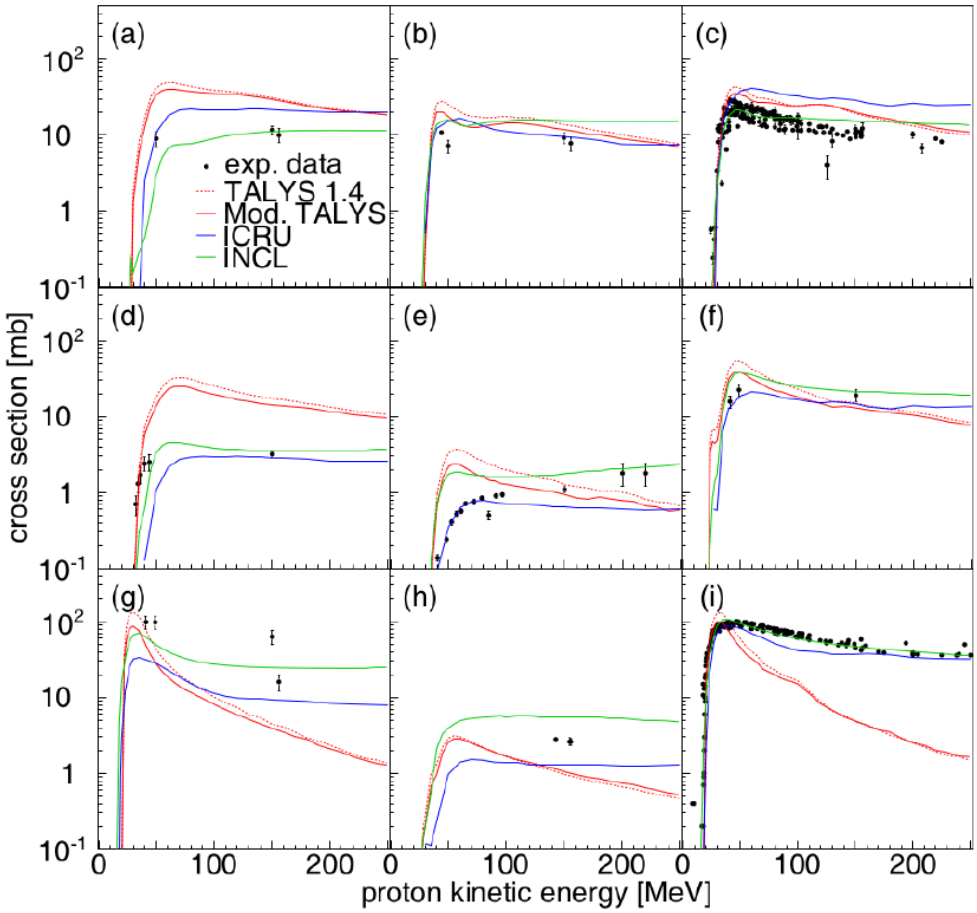

Figure 2.7: Cross section production for different fragments in function to the beam (proton) energy: (a) ^{6}Li, (b) ^{7}Li, (c) ^{7}Be, (d) ^{9}Be, (e) ^{10}Be, (f)^{10}B, (g) ^{11}B, (h) ^{10}C and (i) ^{11}C. Theoretical models are shown in red, blue and green while black data points are visible in all the plots [29].

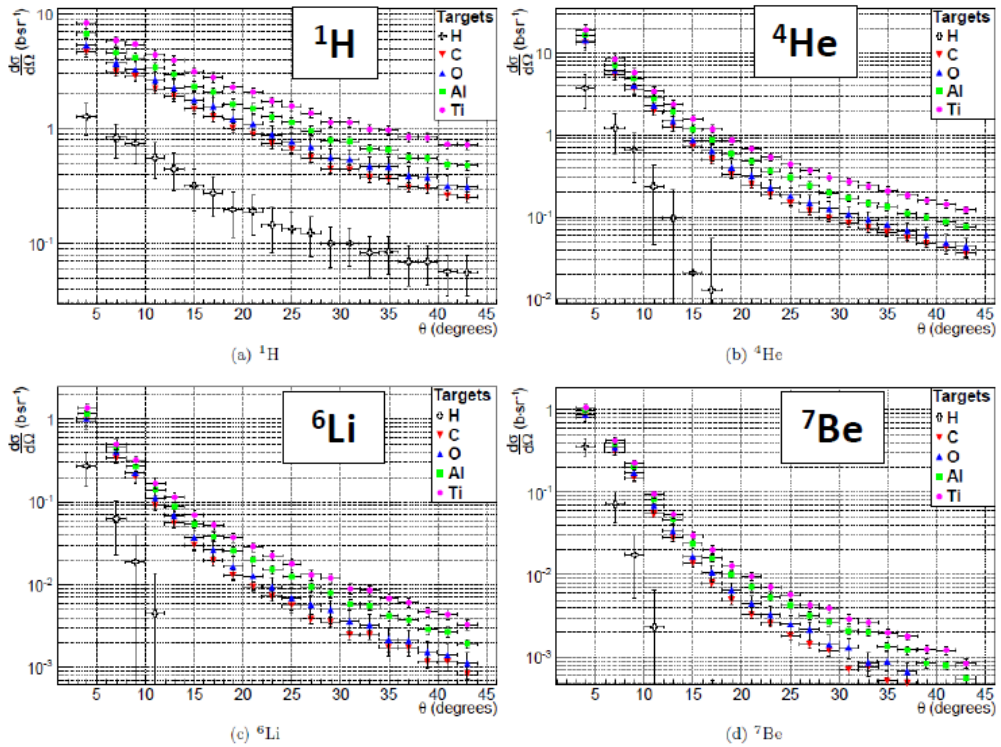

Figure 2.8: Different fragments (H, He, Li, Be) cross section measurement for different targets: H, C, O, Al and Ti [30].

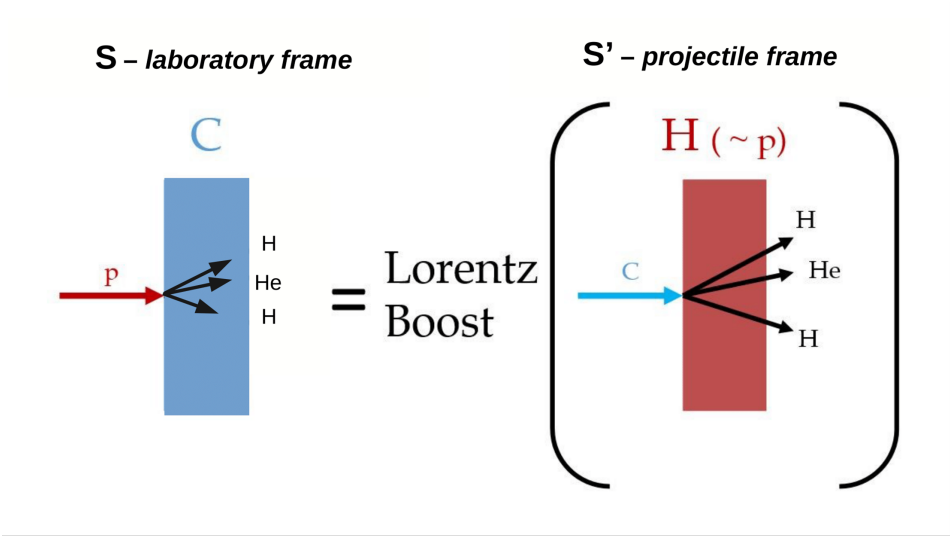

Figure 2.9: Scheme of inverse kinematics approach: laboratory and projectile frame differences are drawn.

Chapter 3

The FOOT Experiment

The FOOT (FragmentiOn Of Target) experiment was designed mainly by INFN in 2017 in order to study nuclear fragmentation in hadrontherapy. The goal of the experiment is the precise measurement of differential nuclear cross sections in order to have a complete set of experimental data, as analyzed in the previous chapter, in the energy range of hadrontherapy and space radioprotection. The FOOT apparatus is designed to detect, to track and to identify charged fragments produced in ion collisions with different targets in order to measure both projectile and target fragmentation. Experimental results of FOOT would be important for both hadrontherapy treatment and shielding in space to protect astronauts [31]. In this chapter experiment characteristics and setup are presented.

3.1 Cross section measurement

The FOOT experiment is composed in a way to simulate charged particle interaction with human body. It is a fixed target experiment where beams of charged ion (protons, ^4He, ^{12}C, ^{16}O) are shot on a target made of H or C.
The main goal of the FOOT experiment is to measure double differential cross section $d^2\sigma/d\Omega dE_{kin}$ with an accuracy better than 5% in the hadrontherapy energy range, namely between 150 MeV/u and 400 MeV/u. As explained in Section 2.4, the inverse kinematics approach would lead to the cross section measurement for target fragmentation. The experiment uses multiple targets such as C or C_2H_4, so the proton cross section can be computed combining the cross sections of the different targets:

$$\sigma(H) = \frac{1}{4} \cdot \Big(\sigma(C_2H_4) - 2 \cdot \sigma(C) \Big) \tag{3.1}$$

However, the cross section obtained in this way is affected by an uncertainty which is the quadratic sum of the ones of the separated targets, therefore very precise measurements are needed in order to reduce errors.

3.2 Detector Design

The design of the detector is driven mainly by the radiobiology outcome requests. The principal challenge is the detection of very short range (order of tens of microns) and very low energy (few MeV) fragments produced by the target fragmentation of the proton beam. To achieve this goal an inverse kinematic approach (2.4.2) is also adopted. The experimental setup is composed in a way to be compact and easily transportable for two main reasons: the different beams needed are available in different treatment and research centers, requiring an easy transportability. Moreover the available experimental and treatment rooms, where ion beams of therapeutic energies are available, have limited dimension. A strong redundancy of the fragment measured properties is required: contemporary detection of momentum, velocity and kinetic energy are needed to study with limited systematics the produced fragments in the energy range of interest. It is hard to achieve the desired acceptance for all secondary fragments with an apparatus of limited size because lower mass fragments (protons, deuterons, etc.) can be emitted within a wider angular aperture with respect to heavier nuclei. Therefore the FOOT experiment implements two different setups:

- an electronic setup, described in the next section, based on a magnetic spectrometer concept in order to identify and measure fragments heavier than ^4He, covering an angular acceptance of $\sim 10^\circ$ with respect to the beam axis;
- an emulsion setup which exploits the emulsion chamber capabilities to measure the production in target fragmentation of light charged fragments such as protons, deuterons, tritons and Helium with an angular acceptance up to $\sim 70^\circ$ [31]. Details are discussed in [32].

3.3 Electronic Setup

The main requirements of the FOOT detector design is a charge and isotopic identification of the produced fragments. For this purpose, the needed physical quantities of the fragments are: momentum (p), kinetic energy (E_k) and time Of Flight (TOF). The detector performances need to achieve the following experimental resolutions:

- momentum resolution $\sigma(p)/p \sim 5\%$
- time of flight resolution $\sigma(T_{tof}) \sim 100$ ps
- kinetic energy resolution $\sigma(E_k)/E_k \sim$ 1-2%
- $\sigma(\Delta E)/\Delta E \sim 5\%$

where the momentum can be measured by magnetic spectrometer composed of magnets and silicon detectors for tracking particles, the fragments charge Z can be identified by energy loss ΔE measurements and TOF through 1.1 using scintillator and silicon microstrips. The mass can be extracted by momentum, velocity β (using ToF) and kinetic energy measurements, provided by Calorimeter, through the following relationships:

$$p = mc\beta\gamma \quad E_k = mc^2(\gamma - 1) \quad E_k = \sqrt{p^2c^2 + m^2c^4} - mc^2 \tag{3.2}$$

where $\beta = v/c$ and $\gamma = \frac{1}{\sqrt{1-\beta^2}}$ are obtained from the fragment TOF.
The detector can be divided in three different regions: the upstream, the tracking region and the calorimeter region (Fig. 3.1).

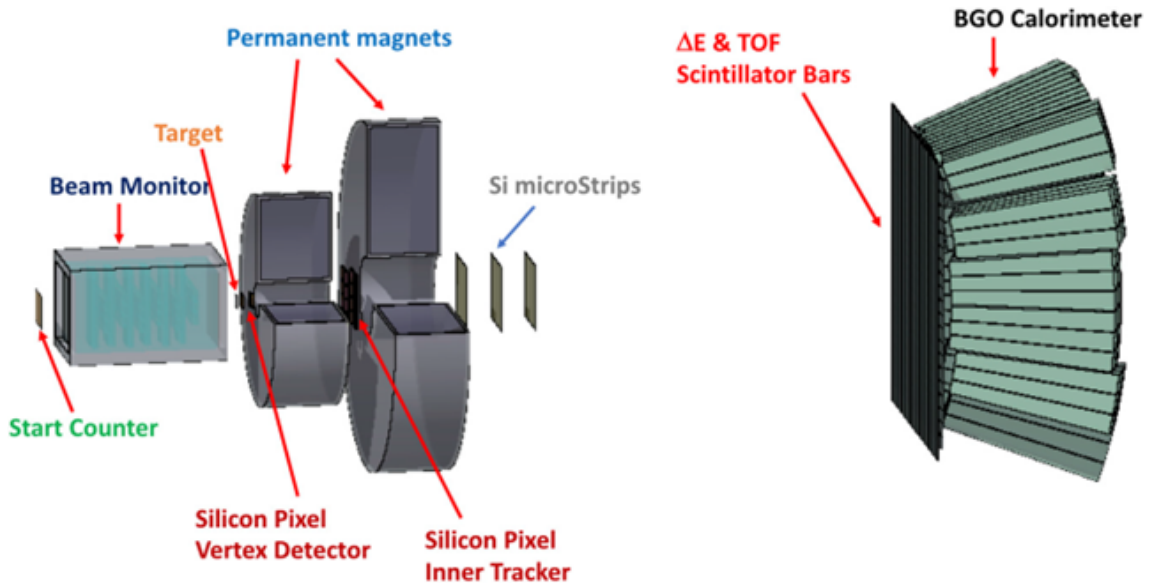

Figure 3.1: Schematic view of the FOOT electronic setup apparatus [33].

3.3.1 Upstream region

In the first part of the detector the beam crosses a thin plastic scintillator counter: the Start Counter. It provides trigger information and the start of the TOF, then a drift chamber acts as beam monitor tracking the beam direction and position. At the end of this region the beam hit the target.

Start Counter

The Start Counter (SC) is made by a 250 μm thick scintillator disk, a EJ-228 fast scintillator foil, with a radius of 26 mm sufficient to cover the typical beam transverse

size. The light produced in the scintillator is collected laterally by 48 3×3 mm^2 SiPMs, 12 per side, bundled in eight electronic channels. A scheme of the detector is reported in left side of Fig. 3.2. The SC is placed 20-30 cm upstream from the target and provides the trigger signal to the whole experiment and also the measurement of incoming ion flux to be used for the cross section measurement. It also brings the reference time for all the other detectors allowing the TOF measurement in combination with the ΔE-TOF scintillator detector. The SC performance gives a time resolution of the order of 50 ps satisfying FOOT detector requirements.

Beam Monitor

The Beam Monitor (BM) is a drift chamber filled with a gas mixture of Ar/CO_2 consisting of 12 layers of wires, with three drift 16×10 mm^2 cells per layer (right side Fig. 3.2). Plane layers are oriented along the x and y axes alternated in such a way to reconstruct the beam profile. The BM detector is placed between the SC and the target in order to measure the direction and impinging point of the ion beam on the target, a crucial information needed to address the pile-up ambiguity in the slow VTX detector. Therefore the BM read-out time, of the order of 1 μs or less, is fast enough to ensure that tracks belonging to different events cannot be mixed. A precision of few hundred μm in the impact point provided by the BM is needed to discriminate the right vertex in pile-up events. This procedure requires a good alignment between BM and VTX. The spatial resolution of 100 μm implies a track direction reconstruction with an accuracy of few mrad, needed for a good resolution in particle identification [31].

3.3.2 Tracking region

The overall tracking system of FOOT is a magnetic spectrometer arranged in three measuring stations. The physical and geometrical needs require the use of monolithic pixel sensors in the two upstream stations Vertex detector VTX and Inner Tracker ITR, while a telescope of silicon Microstrip Detector (MSD) for the most downstream station. In between the three stations, two permanent magnets provide the required magnetic field.

Vertex Tracker

The vertex detector (VTX) is organized in four sensor layers of MIMOSA-28 (M28) chip, a CMOS Monolithic Active Pixel Sensors (MAPS). It is represented in Fig. 3.3. The architecture of the MIMOSA-28 integrates a fast binary read-out and a zero suppression logic to reduce the amount of data produced. Inside the read-out board there is the sensor which consists of a matrix composed by 928×960 pixels of 20.7 μm pitch for a total sensitive area of 20.22 ×22.71 mm^2, giving in overall a material budget for the

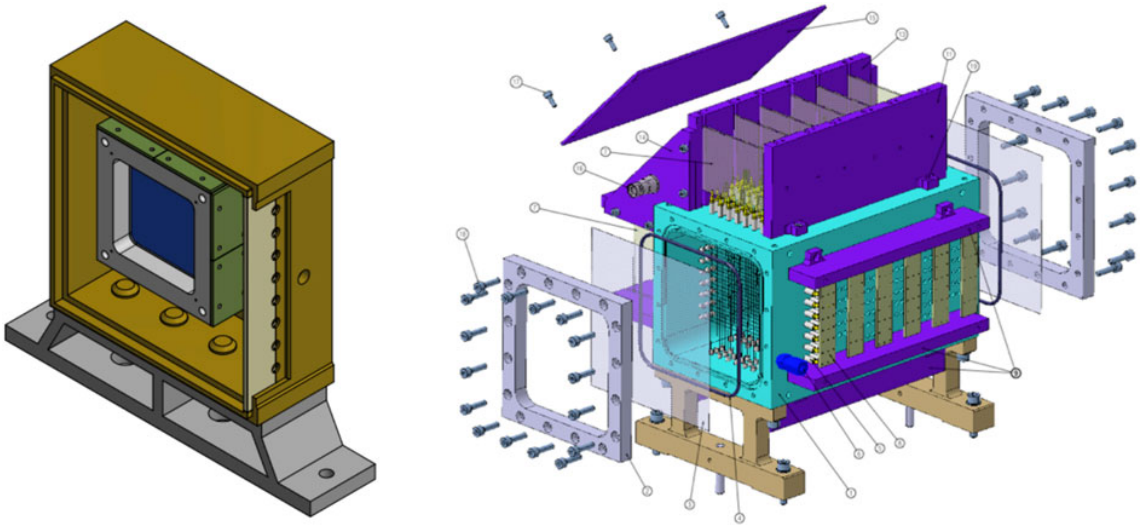

Figure 3.2: Scheme of the Start Counter detector inside the plastic box. The aluminum mechanical structure holds the plastic scintillator foil in dark blue (left). Drawing of the Beam Monitor drift chamber, the two orthogonal x–y views of the wires are clearly visible (right) [33].

entire Vertex tracker of 200 μm. The detector gives an acceptance at the level of about $\pm 40^{\circ}$ with a spatial resolution of 5 μm [31] for the fragments produced in the target.

Inner Tracker

The FOOT Inner Tracker is organized in two planes of pixel sensors, covering a sensitive area of about 8×8 cm^2 in between the two permanent magnets, to measure the position of the track in the plane orthogonal to the beam axis and the direction of the track itself. The fragment spatial distribution is broader at at this point, since the inner tracker is farther from the target (at a distance of about 16 cm) than the Vertex. For this reason, the area to be covered is larger and a different spatial configuration is needed. The tracker is made of two planes of 16 M28 sensors arranged in four ladders (right side Fig. 3.3), In each module the four sensors are glued and bonded on a kapton Flexible Printed Cable (FPC), having two or three conductive planes and an overall thickness of about100 μm. In order to minimize the horizontal dead area the distance between two consecutive sensors in the same module is about 30 μm.

Magnets

An important element for the experiment is the magnetic system used to bend the fragments produced in the target and compute the momentum of particles. The main

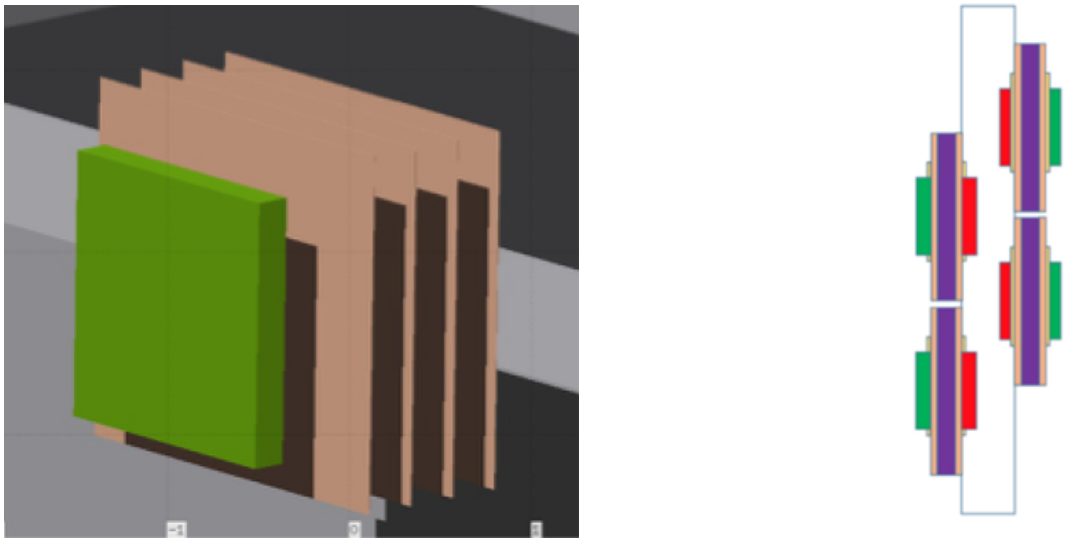

Figure 3.3: Schematic view of target and vertex detector (left). Inner tracker four modules structure (right) [31].

constrains are the momentum resolution at the level of few percent and the portability of the system which forced the choice of permanent magnets producing the needed $B \cdot L$ in a limited sizes and weight. It is formed by two magnets in Halbach configuration: this allows to add the Inner Tracker inside the magnetic field. The first magnet has a gap diameter of 5 cm while the second one of 10.6 cm, providing respectively a maximum intensity of 1.4 T and 0.9 T along the y axis in the internal cylindrical hole. Each magnet is made of twelve single units of Samarium-Cobalt which maintains its magnetic properties also in high radiation environments. Thanks to a detailed field map (Fig. 3.4), it is possible to reach the intrinsic achievable accuracy of $\sim 10\,\mu$m.

Microstrip Silicon Detector

Tracking of fragments downstream the magnetic volume is essential for the measurement of momentum and to match the reconstructed tracks with the hits in the ToF scintillator and the calorimeter. That is why after the second magnet is located the Microstrip Silicon Detector (MSD) which provide also a redundant measurement of dE/dx to improve the reliability of the experiment. To detect ions with $Z > 2$ an angular opening of 10° is set with a coverage surface of 9.3×9.3 cm^2. The detector is composed of three x-y planes (left Fig. 3.5) separated by a 2 cm gap along the beam direction in order to reduce the amount of material. Each plane is formed by perpendicular Single-Sided Silicon Detector (SSSD) with a thickness of $50\,\mu$m to minimize further fragmentation and a readout pitch of $150\,\mu$m for a spatial resolution lower than $40\,\mu$m. The MSD is

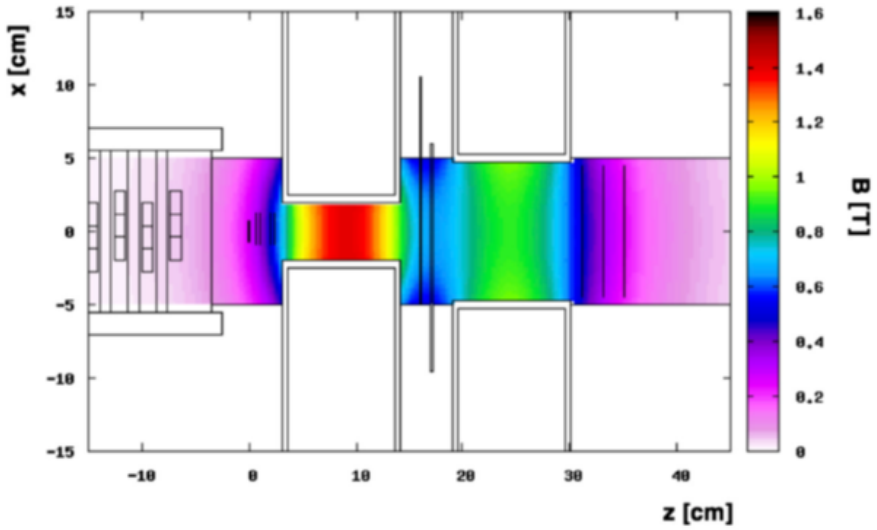

Figure 3.4: Magnetic field map produced by magnets in Halbach configuration. The magnetic field intensity B, shown in the palette, is referred to its y-axis component [33].

the main focus of this thesis, a more detailed description of this detector is reported in the next chapter (4.3).

3.3.3 Downstream region

The last region of the electronic apparatus, located at 1 m distance from the target, is composed of two detectors: ΔE-TOF (or ToF Wall) and the BGO calorimeter.

ToF Wall

The ToF Wall detector provides the stop to the Time of Flight and the measurement of the energy release ΔE in a thin slab of plastic scintillator to identity the charge of the crossing fragment. It is made of two orthogonal layers of 20 plastic scintillator bars, each one 3 mm thick, 2 cm large and 44 cm long (right Fig. 3.5), coupled at both ends to silicon photomultipliers (SiPM) which have 3×3 mm^2 of active area and a pitch of 25 μm.
The bars thickness is a compromise between the accuracy of ΔE measurements and the effort to reduce the secondary fragmentation probability. The layout and readout allow a dE/dx measurement accuracy of $\sim$ 5% and a TOF resolution better than 100 ps for the nuclear fragments.

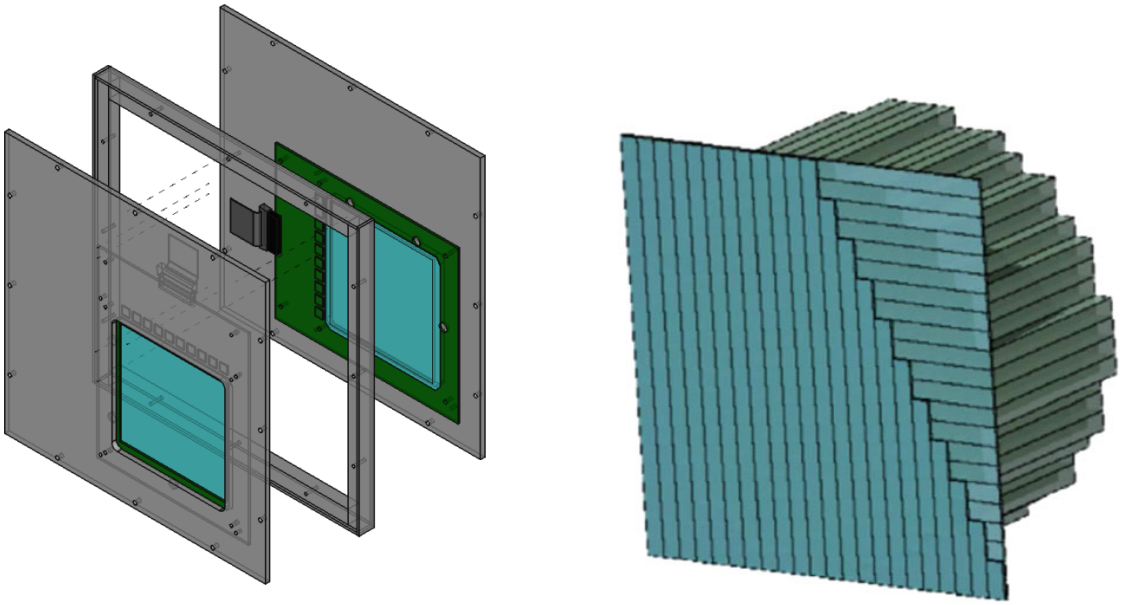

Figure 3.5: Exploded view of one of the x-y stations of the MSD (left). Schematic view of the fragment identification region: the two orthogonal layers of 20 plastic scintillator bars (ToF Wall) in front of the BGO Calorimeter crystals matrix (right).

Calorimeter

The last detector in the apparatus is the Calorimeter which is designed to measure the total kinetic energy of projectile fragments. The upper bound of the fragments energy range is defined by the beam energy, while the lower bound is set by the intensity of the magnetic field.
The experiment works at a relatively low beam intensity, therefore the chosen material for the calorimeter is BGO: a dense crystal, with high light yield, without strict requirements of the response speed. It covers a circular surface of about 20 cm radius, which corresponds to about 350 BGO crystals (right Fig. 3.5) with an active surface of 2x2 cm^2 and a single sensor pitch of 15 μm, coupled to a matrix of 25 SiPM.
Each crystal has a truncated pyramid shape, with a length of 24 cm and a front and back size of 2×2 cm^2 and 3×3 cm^2 respectively. The dept of each crystal has been chosen in order to minimize the energy leakage due to possible hadronic showers which can be produced and not fully contained in the detector.

Chapter 4

Analysis

The goal of this thesis is the improvement of the clustering algorithm relative to the MSD detector. It has been performed on sample relative to the following data taking campaigns at GSI in July 2021 and CNAO in 2022. The complete list of the analyzed data is reported in Tab. 4.1. In this chapter the following topics are presented: data taking layout and specifics, the software used for the analysis and the study made on the MSD detector. It will also be described the main ideas behind the studies done in this thesis, namely on MSD noise treatment and charge mitigation among strips.

4.1 Data Taking

4.1.1 GSI 2021

The GSI facility, located in Darmstadt (Germany), is a research center chosen for the FOOT experiment data taking. It is equipped with a heavy ion accelerator used for nuclear structure and reaction experiments [34]. It is composed of a linear accelerator of 120 meters length, followed by a synchrotron with a circumference of 216 meters. In July 2021, some measurements were performed by the FOOT experiment with a partial setup composed by: the Start Counter, the Beam Monitor, the Vertex, the Micro Strip Detector, the ToF Wall detector and 9 of the 320 BGO crystals of the calorimeter (left side Fig. 4.1). The missing systems were still under construction, in time with the expected deadlines. The target were made of both graphite (C) and Polyethylene (C_2H_4). A beam of ^{16}O at energies of 200 MeV/u and 400 MeV/u was used, for a total of more than 40 millions events in several configurations. The main drawbacks of the FOOT setup at GSI were the absence of the magnets, which means no momentum reconstruction, and the reduced BGO configuration allowing for kinetic energy measurement with a limited angular acceptance. This data acquisition was fundamental for several detector studies and for preliminary fragmentation cross section measurements. The GSI 2021

run analyzed in this study is an alignment type using ^{16}O of 400 MeV with no target involved.

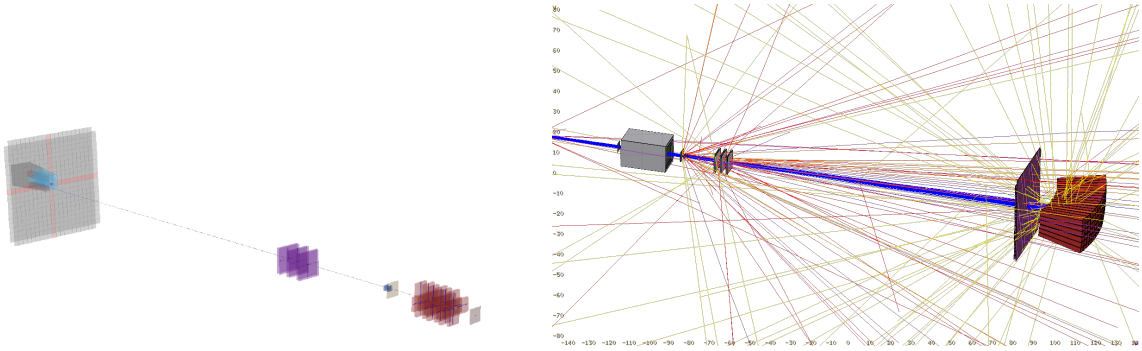

Figure 4.1: FOOT experiment setup for GSI 2021 (left) and CNAO 2022 (right) [35].

4.1.2 CNAO 2022

The National Center for Oncological Hadrontherapy (CNAO), based in Pavia, is one of the six facilities around the world that uses hadrontherapy with both protons and carbon ions to treat tumors. At CNAO there are two devices called "sources" from which the particles beams for the hadrontherapy sessions are generated. These atoms are extracted: protons and carbon ions are selected and "bundles" of beams are created. These bundles are sent to the synchrotron where they are accelerated to kinetic energies up to 250 MeV for protons and 200-300 MeV/n for carbon ions. Finally they are sent to the three treatment rooms. The FOOT experiment setup in 2022 campaign included the Start Counter, the Vertex, the Micro Strip Detector and twelve 3x3 calorimeter modules (right side Fig. 4.1). The target was made of graphite (C) with density of $1.83\,\mathrm{g/cm^3}$.

Campaign	Dataset Number	Type	Beam	Energy
GSI2021	Run 4313	Alignment	^{16}O	400 MeV
CNAO2022	Run 5300	Alignment	^{12}C	300 MeV
	Run 5468	Physics	^{12}C	200 MeV

Table 4.1: Analyzed datasets list. First three columns indicates: the reference campaign, the run number and type. The last two columns reports beam type and energy.

4.2 Software: SHOE

The software framework developed for the FOOT experiment is SHOE (Software for Hadrontherapy Optimization Experiment): it is a C++ software based on ROOT

framework [36], designed to perform reconstruction steps for all subsystems, both for MC simulations and real data. It is maintained by the FOOT collaboration using a git repository provided by INFN [37].

4.2.1 Simulation

The FOOT simulation has been built in the framework of the FLUKA code [38]. FLUKA is a Monte Carlo transport simulation code tested through the comparison with many experimental data and adopted in many physics fields of study such as particle, nuclear and medical physics.
To run the simulation, the user must provide a description of the setup and some physical specifications, which have to be included in configuration and geometry files. The MC code generates beam particles, energy losses, nuclear interactions and fragmentation with their kinematic quantities: momentum, velocity, initial an final position. All the results are finally stored in ROOT format files.

4.2.2 Reconstruction

The reconstruction software package handles the decoding of the data and simulation events, building in two main steps (*Level 0* and *High Level*) all the necessary input information to perform a full event reconstruction and data analysis:

- *Level 0*: The first step consists in reading, interpreting and converting in a single software-object format both the data and the simulation events provided in different input formats. The signals collected during the data acquisition runs are decoded, the detector dependent calibration constants are applied and the output of each detector is organized in *Hit*, *Cluster* and *Track*. An *Hit* is the signal recorded by detector elements (such as pixel, strip or wire), a *Cluster* is a group of adjacent hits composed in different ways depending on different detectors of FOOT. Lastly, a *Track* is the reconstruction of the path taken by a charged particle in a detector, formed by combining information from different clusters along the particle's trajectory.

- *High Level*: In a second step, events are processed by track identification and reconstruction algorithm. The different fragments are identified and their cross section estimated.

4.3 MSD: state of the art

As explained in 3.3.2, the Micro Strip Detector (MSD) is important both to track fragments and to measure *dE/dx*. A charged particle passing through the silicon sensor

deposits energy along the track creating electron-hole pairs (left Fig. 4.2), then the charge carriers drift toward the electrodes to be collected. The microstrip silicon detector is made of 1920 identical silicon strips extended along one axis for a total active area of 96 $\times$ 96 mm^2 with 150 μm thickness of the active layer (right Fig. 4.2). The signal from the floating strips is transferred by capacitive coupling to the readout strips, improving the resolution with a smaller number of readout channels, as detailed in this chapter.
In FOOT experiment there are 3 measurement layers of MSD, each one composed of two x-y planes orthogonally oriented. Since silicon detectors are sensitive to visible light they have to be shielded, to this purpose the two metallized sides of the detectors are positioned on the external side of an x-y plane structure. Each plane provides space points (x, z) and (y, z) of the nuclear fragment tracks. When a charged particle hits the detector, due to the interaction with the silicon material, an analog signal is generated on the corresponding channel. The generated signal is then preamplified, shaped, sampled and held by an IDE1140 integrated circuit [39].

This chip designed by IDEAS (Integrated Detector Electronics AS) is a 64 channel low-noise/low power high dynamic range charge sensitive preamplifier-shaper circuit. Since each detector has 640 strips and each IDE1140 has 64 input channels, for each single coordinate microstrip detector 10 chips are required. The VA chips are separated into two independent readout groups: the two groups are read in parallel while the VAs of a same group are serially readout [40].

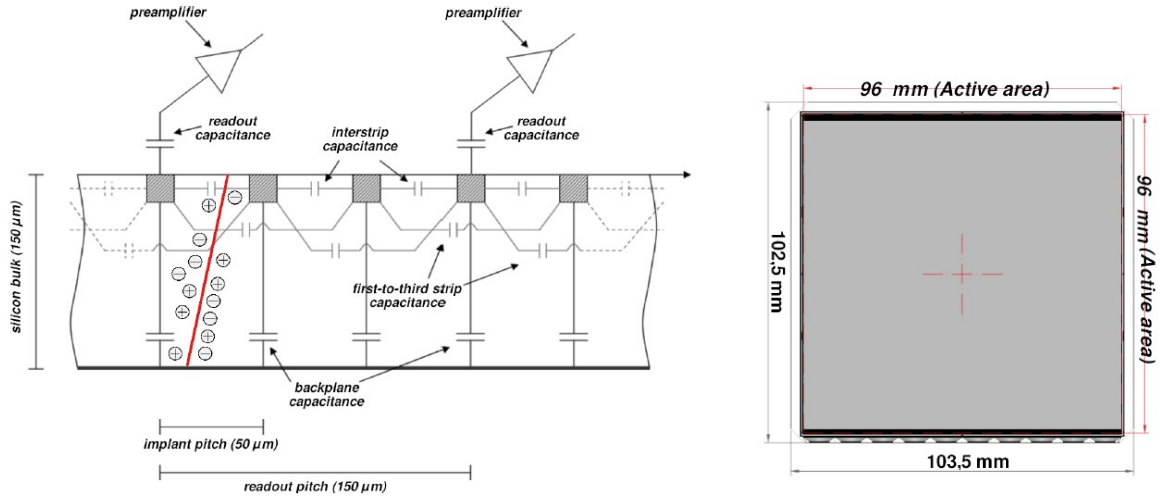

Figure 4.2: Silicon sensor: electric scheme with incident charged particle (left) and technical drawing (right).

Signal and Noise components

As explained in Chapter 1.1.2, the total ionization charge depends on the particle type, on the energy and on the detector thickness. The signal distribution presents an asymmetry with a tail for high energy. In order to obtain charged particle signals, it is of fundamental characterize also the noise of the detector.
The average response of the single strips in the absence of an external radiation source has to be determined and then subtracted to equalize the single strip response. The average noise value is called *pedestal* of a channel and is defined as

$$ped_i = \frac{1}{N}\sum_{j}^{N}(ADC_{ij}) \tag{4.1}$$

where ped_i is the pedestal of channel i, j is the event number, N is the number of events used to compute the pedestal and ADC_{ij} is the raw signal of strip i for an event j.
The external electromagnetic noise could produce a collective signal variation event by event, also this contribution must be subtracted from the raw strip values. The common mode noise (CN) is the average deviation, event by event, from their pedestals of all the channels read by a single ASIC [41]. Hence common mode noise (CN_j) of event j is calculated as:

$$CN_j = \frac{1}{N_j}\sum_{i}^{N_j}(ADC_{ij} - ped_i) \tag{4.2}$$

where N_j is the number of good strips within the ASIC.
The last operation, after pedestal and common mode fluctuations subtraction, is the computation of single strip noise σ_i. This information is crucial to define a uniform criteria (strip signal higher than a threshold) to evaluate if a signal is due to a noise fluctuation or not. The final reduced signal value for each channel is thus [42]:

$$r_{ij} = ADC_{ij} - ped_i - CN_j \tag{4.3}$$

4.4 Clustering Algorithm

If a charged particle pass through the region between two strips, the charge collection and signal formation are split in a non trivial way into the readout of the two closest connected strips. Hence an algorithm to reconstruct these signals, even if split among several adjacent strips, is needed. At the end, it will produce a cluster object as physical observable quantity.
The reduced signal r_{ij} (4.3) allows checking if a signal is over the noise level. The algorithm acts using a fist "seed" threshold T_s and a second "fire" threshold T_f:

- firstly the algorithm analyzes the reduced values for one event and search the cluster seed which is defined as a channel with $r_{ij} > T_s$ (Fig. 4.3)
- when the cluster seed is found, adjacent strips are checked for values over the fire threshold, until $r_{ij} < T_f$.

Both T_s and T_f threshold values are expressed in terms of single channel signal over noise (S/N) values. In fact for every data taking there are different thresholds depending on the setup: for GSI 2021 T_s is 50.0 and T_f is 30.0, while for CNAO 2022 T_s is 5.0 and T_f is 2.0. The second threshold has a lower value because strips are coupled, therefore the particle should induce signal in more than one strip.
The main properties of a cluster are the position, the deposited charge and the signal width. The position is the expected position of the incoming charge a particle, the charge is obtained by the sum of the analog *dE/dx* signals of each strips composing the cluster and the width is the number of strips included in the cluster.
In Fig. 4.4 are reported two extreme cases of cluster composition for a particle arriving perpendicular to the sensor. In the first case a particle hits in the center between two strips: the signal would be induced in almost equal part in both strips. The cluster width is two. In the second case the particle hits a readout strips: the most part of the signal is induced in that strip and part of the signal is present also on adjacent strips. Here the cluster width is three. This process of cluster composition could fail in some cases due to the strips layout in the detector, this lead to a problem especially for cluster with two strips wrongly reconstructed, as explained below.

4.4.1 Charge migration in floating strip coupling

In a floating strip configuration, part of the current will be absorbed by unconnected strips so the signal on cabled strips will be different, generally lower, then what could happen in a connected configuration [44]. This signal division depends on the track's position with respect to the electrodes, the number of floating strips and their characteristics. The parameter eta (η) is defined as the center of gravity of the two highest readout strips in the cluster:

$$\eta = \frac{S_L}{S_L + S_R} \tag{4.4}$$

and it is used to correct the induced charge on the strips. Where S_L and S_R are the two highest signals in the cluster. Top part of Fig. 4.5 shows as an example the cluster amplitudes for 400 MeV/u incident Carbon as a function of η. The difference in the values between the floating strips and the readout strips shows a charge loss up to approximately 50% for ions at 400 MeV/u hitting near a floating strip, as shown in bottom part of Fig. 4.5 for carbon case. From energies around 200 MeV/u, the measured charge loss appears to decrease respect to the deposited energy of the particle. This behaviour

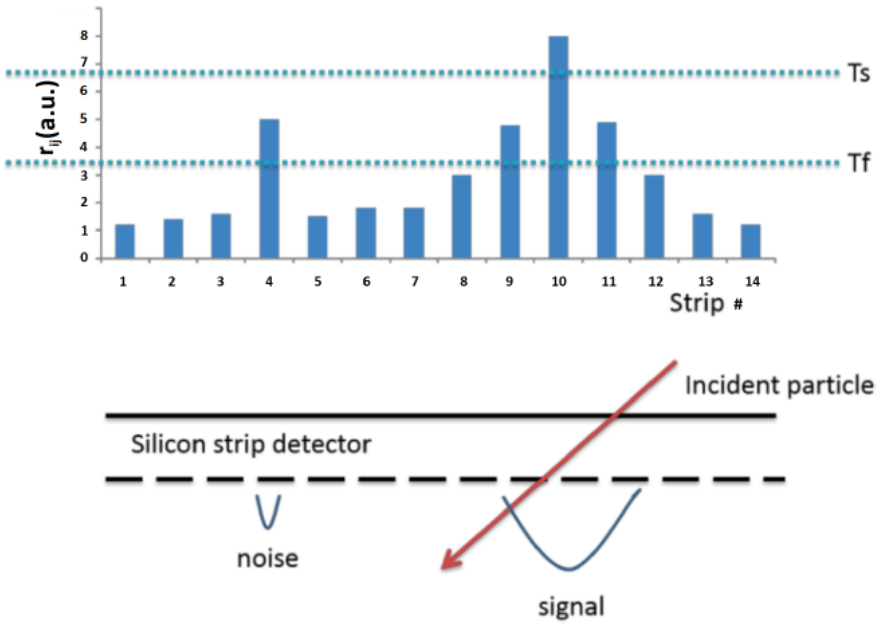

Figure 4.3: Drawing of the clustering algorithm with the two threshold T_s and T_f to discriminate single strip channel [43].

suggests the presence of a saturation regime of the readout electronic: assuming that the single readout channel saturates at a certain energy, the reconstructed clusters for particles hitting near a readout strip will all have similar ADC content, even for increasing deposited energy. On the opposite, clusters from particles hitting near a floating strip that experience charge collection loss will have single channel values below the saturation level that increase with increasing deposited energy. The two effect combine to give a charge loss fraction that decreases with the incoming particle energy. It is necessary to take into account these effects into the signal recombination process in order to avoid bias and improve efficiency.

The effect of the capacitive coupling gives rise to the presence of peaks in the η distribution shown in Fig. 4.6. The resulting charge division between the strips is thus non linear. These peaks give rise to regions which can be used during analysis: readout, floating and intermediate region. The correlation between the strip implantation structure and the peaks of the η is evident, with peaks around 1/3 and 2/3 of the region in between two readout strips. A value of η close to 0 or 1 corresponds to the readout strip incidence, while η values close to 0.3 or 0.7 correspond to the floating strip incidence [43]. This effect causes a problem when a particle passes between two readout strips ($\eta \sim 0.5$): the strips which should be signal type are below the noise threshold due to the charge loss. The cluster is reconstructed incorrectly by the double threshold algorithm because a strip could not be considered. In case of an expected cluster with two strips, the loss

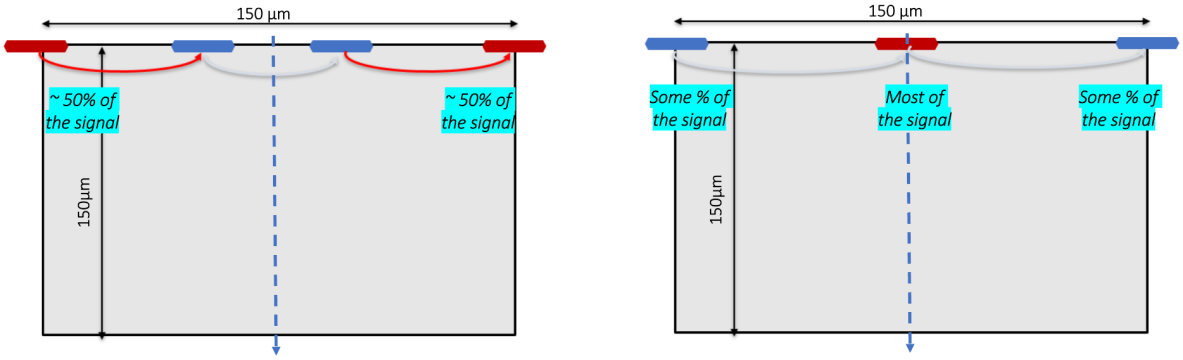

Figure 4.4: Track of a particle (blue dashed line) impacting on the detector at 90°. Two cases: between two strips (left) and on a strip (right).

influences the algorithm reconstructing a cluster with only one strip leading to a spatial resolution equal than digital case and the inability to define η.
Handle this loss, improving the clustering algorithm, is the focus of this thesis.

4.4.2 Improvement Strategy

The study is carried out can be divided in two parts: a software implementation of the clustering algorithm and a following application to the η correction map, processed with different datasets. The results of this analysis are collected in Chapter 5.

Software work

In order to reduce the signal loss described above, two changes (acting after the two threshold steps) have been performed in the clustering algorithm:

1. to define correctly η at least two strips are needed, as 4.4 suggests. Due to the loss presented above the algorithm could reconstruct a cluster with less number of strips, also with only one strip. In this cases η can't be correctly defined. In order to avoid this problem, two strips are always added at two ends of the cluster(Fig. 4.7). In this way clusters have always at least two strips and η is set.

2. handling of noisy strips which are removed only at the end of the clustering procedure, while in the previous version they were simply skipped and not considered. This will led to a wrong cluster description in case of a noisy strip next to the seed with values over T_f threshold.

In the first change an important exception was to exclude an addiction for the first and the last strip, because a strip can't be added before the strip number 1 and after

VA	Gain
0	1.000000000
1	0.996448023
2	1.008287947
3	1.019417476
4	1.005209567
5	1.030073408
6	1.124911201
7	1.103362538
8	1.090812219
9	1.127634383

Table 4.2: Gain values to correct cluster signal: the first columns identifies the 10 VAs of a sensor. While the second reports the applied values.

the strip number 640. In these specific cases only one strip is added to the cluster.
The strategy of second change consisted in adding also noisy strips in cluster if near a seed strip with signal. That is important because if a noisy strips over T_f threshold is completely skipped, double threshold algorithm does not find a second strip to consider in the cluster and again η can't be defined with only one strip.

η correction

In order to correct the loss in intermediate η region, a correction on cluster signal is needed. Each VA chip exhibits different response, therefore cluster signals need to be corrected with the so called *gain factors*: they are different depending on the sensor and on the VA chip in a sensor. The procedure for gain estimation consists in evaluate the peak position for each Z and for each VA of every sensor selecting the readout region. Finally, compare the results with a chosen reference and evaluate the gain factors. As an example, in Tab. 4.2 are reported VAs corrections for the first sensor of the MSD: all values refers to the first VA of the sensor which is thus equal to one.

The second step is to apply the correction depending on η through the correction map. This was taken from results obtained with the SSD prototypes tested in November 2022 at CERN for HERD experiment [45]. The correction map (Fig. 4.8) needs two variable in input to be computed: the cluster $\sqrt{ADC}$ and η. Once they're obtained, the map gives a correction value corresponding to their values. In particular an x-y $(\eta - \sqrt{ADC})$ interpolation procedure was performed to obtain the correction value which is applied, for every sensor of the MSD, to the cluster $\sqrt{ADC}$ in order to reduce the charge loss described above. The map suggests that the correction values for extreme η, corresponding to readout region, are smaller compared to cluster with central η which

η	$\sqrt{ADC}$	Correction
0.0121	48.915	1.0000
0.28194	39.89361	1.3641
0.5046	41.178	1.3935
0.70926	40.8472	1.3641
0.9884	50.458	1.0000

Table 4.3: Correction values applied to cluster $\sqrt{ADC}$ for different η values.

correspond to intermediate region. As it is expected because the signal loss is more evident in this region. All values obtained from the map are rescaled respect to the correction values at $\eta = 0$ and $\eta = 1$ in order to obtain values equal to 1 for readout regions. Some corrections in readout, floating and intermediate region of η are reported in Tab. 4.3 as a reference.

SHOE software implementation

Changes in the algorithm and η corrections are integrated in the SHOE software, in order to be applied in the data analysis. As mentioned in 4.2.2, the software code is divided on different levels, the improvements described above are implemented in *Hit* and *Cluster*. The actual MSD double threshold algorithm adopts a specific workflow adapted from VTX detector clustering: once a cluster seed is found, the cluster finding function searches for all the neighbour strips to the seed strip in an iterative way, not considering completely the noisy strips. The change 1 is carried out in the *Hit* level of the code: once the sensor, the strip number and the ADC value are known, the software can add a chosen strip to the *Hit* object. Here two strips are added, one before the first and one after the last strip in the cluster, requiring that these strip are not correspondent to noisy strips.
Afterwards, in the *Cluster* level of the software, the change 2 is implemented: noisy strips are now added to the cluster (if they are present), but not considered for computing cluster properties like position and energy.

For the η correction there are two steps: gain factors application and the signal values correction, both carried out in the *Cluster* level.
For the first step, the gain factors are used once the correct sensor and VA chip are selected. The gains file consist in 60 values divided for each sensor and each VA. An example for the first sensor is reported in Tab. 4.2. Once this new signal values are obtained, the η correction is applied: in this case the values are taken from a calibration file which reports η, $\sqrt{ADC}$ and the correction. These values are compared to the cluster signal computed in the software to find the corresponding correction to apply.

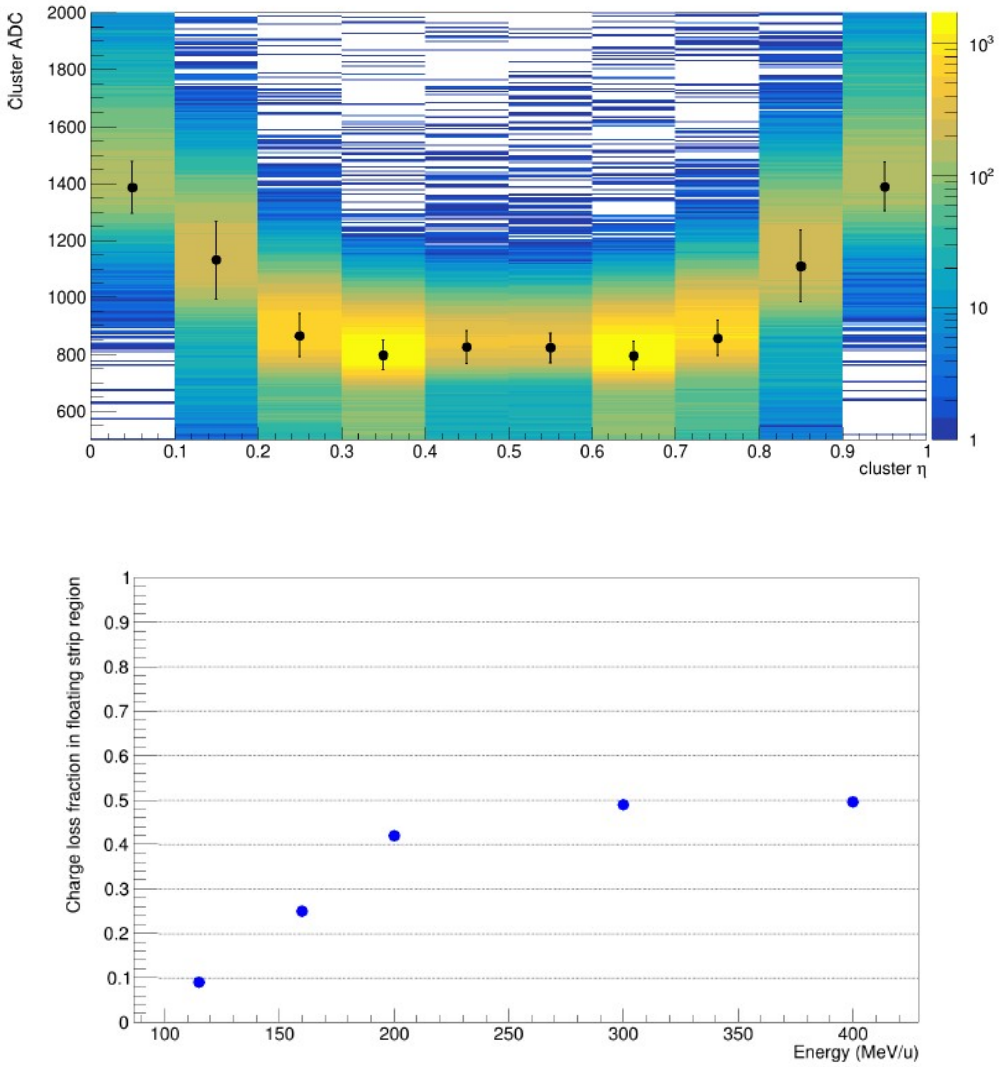

Figure 4.5: Cluster ADC as a function of η for 400 MeV/u carbon: the signal loss is visible between two readout strips (top). Charge loss fraction of clusters in the floating strip region in function of the carbon energy (bottom) [43].

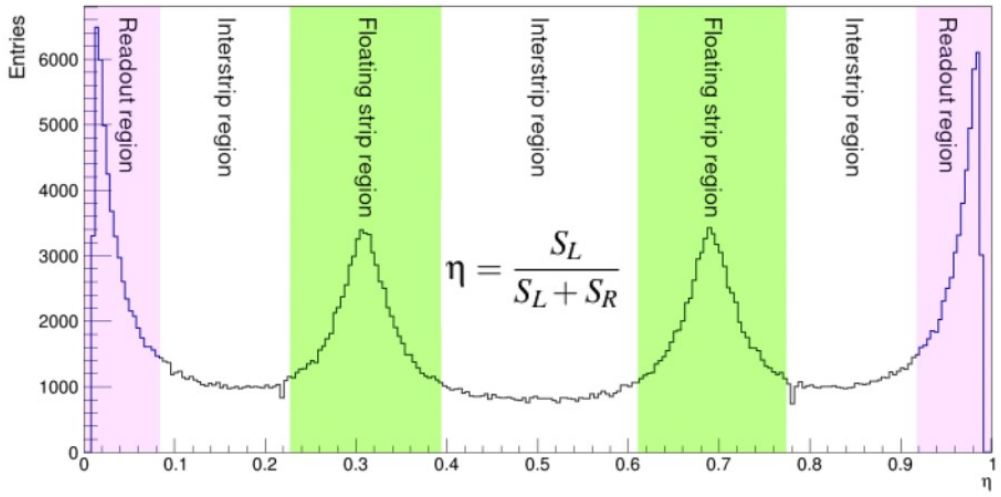

Figure 4.6: Different regions for η distribution: reading, intermediate and floating region [43].

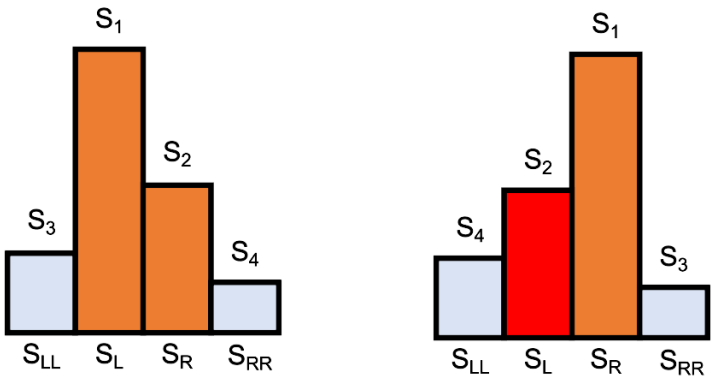

Figure 4.7: Example of cluster with changes adopted: S_L and S_R (in orange) are the strips above the two threshold, while S_{LL} and S_{RR} in grey are the added strips by new algorithm(left). Noisy strip next to the cluster seed is highlighted in red (right).

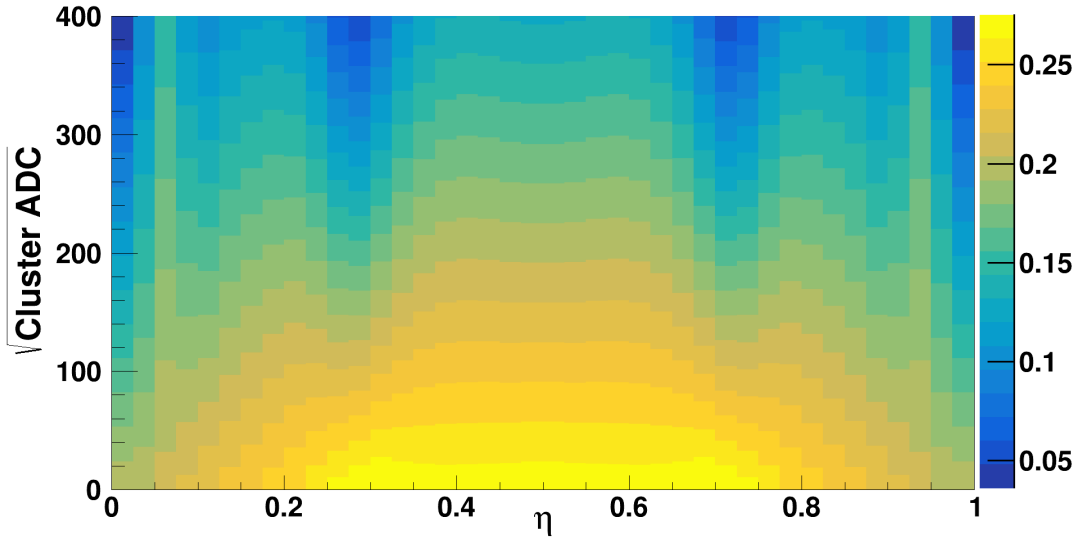

Figure 4.8: η correction map used to correct $\sqrt{ADC}$ in function of η parameter. The colors represent the different correction for each value, on the right the reference palette.

Chapter 5

Results

The main results obtained through the implementation presented in the previous chapter are shown here. The changes adopted in the algorithm are analyzed using data from GS12021 campaign. Then CNAO 2022 data are taken into account to check the reliability of η correction on a different campaign.

5.1 Algorithm changes

In Fig. 5.1 the cluster width, namely the number of strip in a cluster, before and after the changes adopted are reported. For utility are defined three cases:

- *case 1*: original version of algorithm (top plot);
- *case 2*: two strips are added: one on top and one on bottom of the cluster (center plot) in order to define correctly η (as explained in 4.4.2);
- *case 3*: change of *case 2* is implemented and the noisy strips are considered in the clustering and handled (bottom plot).

It is clear the presence of a difference of two strips between clusters size in *case 1* and *case 2*: all values are shifted by two bins due to the addition made. In this way there is no possibility to have clusters with less than 2 strips and the cluster center of gravity can be found with a better precision.
The difference between *case 2* and *case 3* is visible mainly for few cluster: it is more evident in Fig. 5.2 where the ratio of number of clusters between *case 2* and *case 3* are presented. Considering also noisy strips clusters have larger width, namely clusters with few strips are merged together to form clusters with higher number of strips. In original version of the algorithm, noisy strips were not considered leading to obtain an higher number of clusters with lower number of strips. Therefore the number of clusters with 2,3 and 4 strips in *case 3* decrease having a ratio of (0.32 ± 0.02), (0.72 ± 0.01) and

(0.92 ± 0.01), while the number of clusters with 5 and 6 strips have a little increase with ratios just above 1. Looking at the number of entries in all the histograms, there is a decrease in the number of total clusters between *case 2* and *case 3*, consistent with the merging of clusters with few strips.

The implemented changes are checked also for another property: the cluster position, namely the measured position of the incoming charged particle. It is shown in Fig. 5.3 for the first two sensors, comparing *case 1* (red) and *case 3* (blue). A Gaussian fit is computed in order to highlight the difference of distributions between the two cases. The position is expressed in cm where the 0 represents the center of the sensor, namely the strip n.320.
In sensor 1 for *case 1* the mean value of position is (0.3829 ± 0.007) cm, while for *case 3* it is (0.3943 ± 0.007) cm. There is an increase of the order or 2.9%. The σ reduces from (0.1724 ± 0.005) cm to (0.1627 ± 0.005) cm.
While in the sensor 2 for *case 1* the mean value of position is (0.3433 ± 0.007) cm, while for *case 3* it is (0.3604 ± 0.007) cm. There is an increase of the order or 4.7%. The σ reduces from (0.1746 ± 0.005) cm to (0.1609 ± 0.005) cm.

Once the clusters are computed, the software proceeds to compose the *Points*, which are the (x,y,z) cluster coordinates for each MSD station. These are obtained by considering the clusters formed in the x and y layer of each station. The difference between *case 1* and *case 3* in x-y plane for the points are illustrated in Fig. 5.4. The cluster position increase reflects also on coordinates of the points.

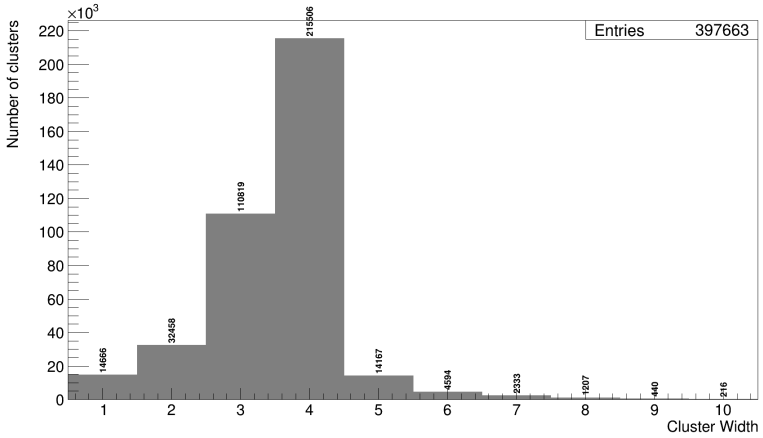

Case 1

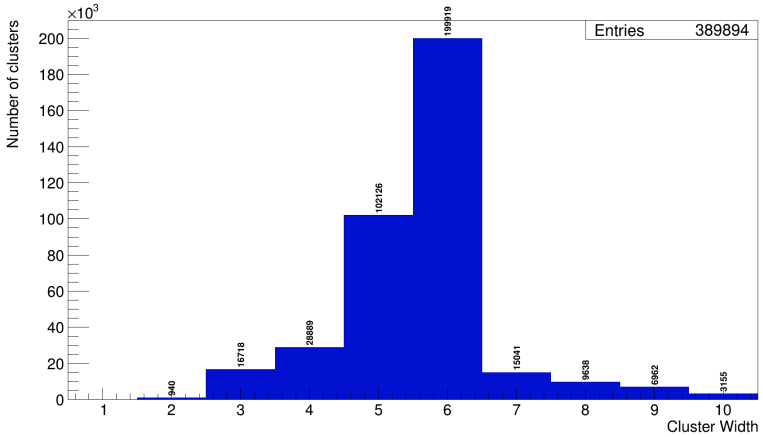

Case 2

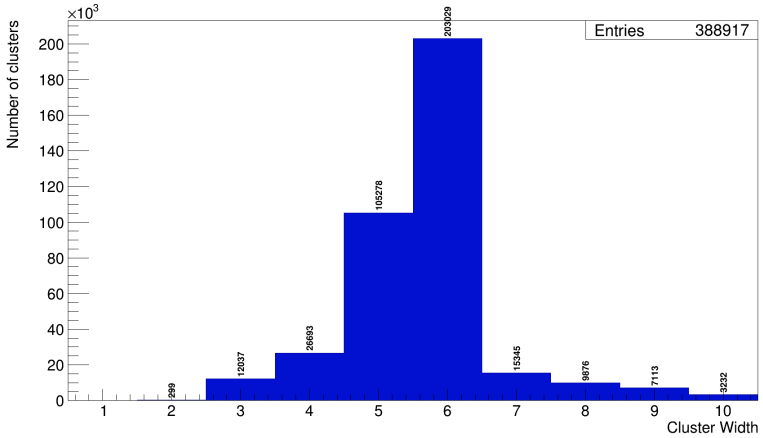

Case 3

Figure 5.1: Number of strips per cluster for *case 1* (top in grey), *case 2* (center) and *case 3* (bottom). The number of cluster for each width are indicated on top to compare different cases.

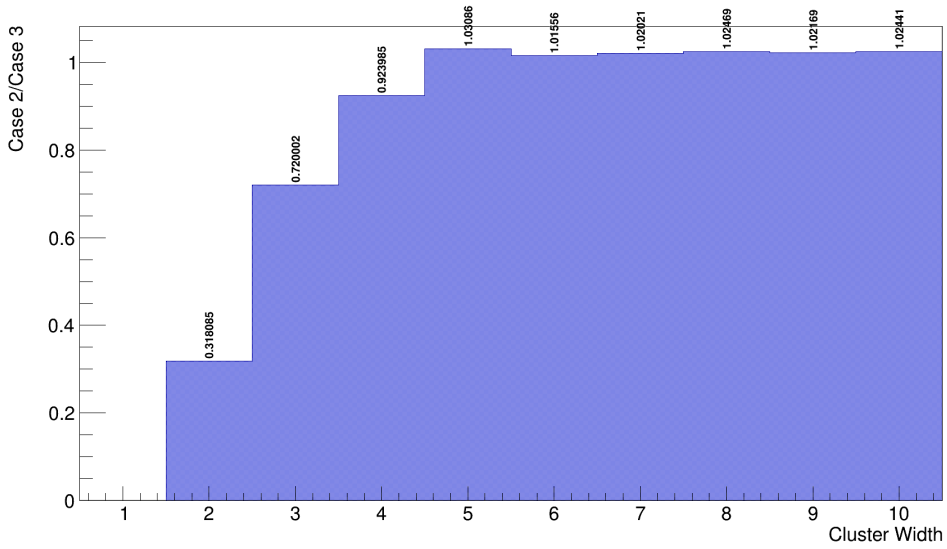

Figure 5.2: Ratio of number of clusters between *case 2* and *case 3*. The values are indicated on top of each bin.

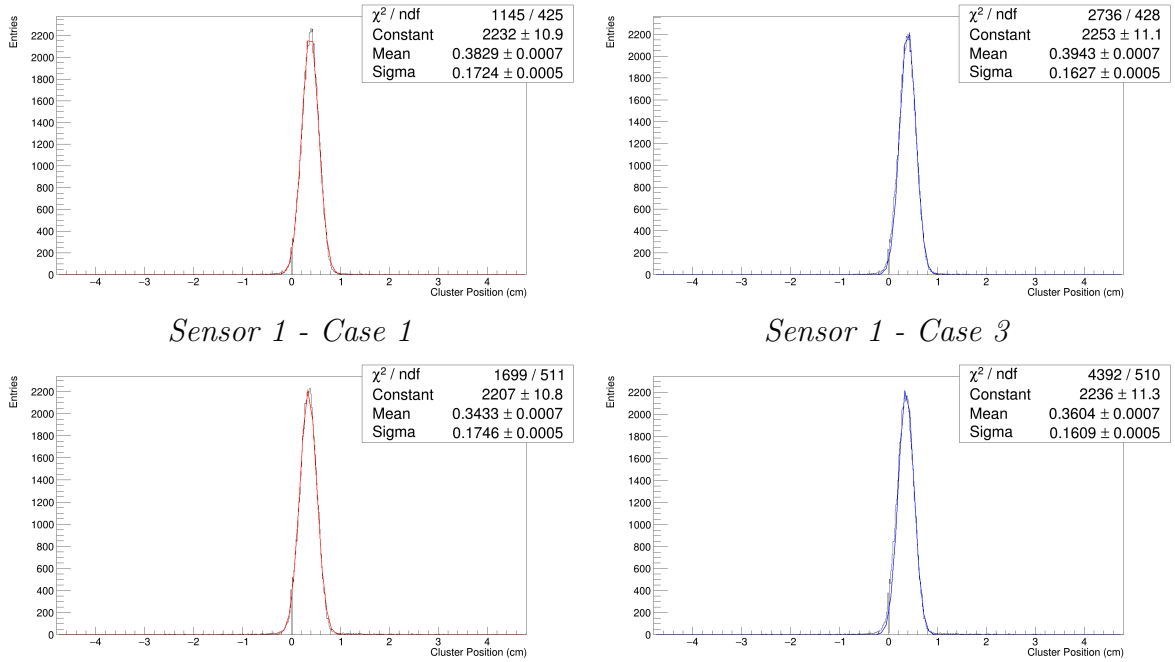

Figure 5.3: Cluster positions in sensor 1 (top) and 2 (bottom). For each one *case 1* (left in red) and *case 3* (right in blue) values are fitted using Gaussian distribution.

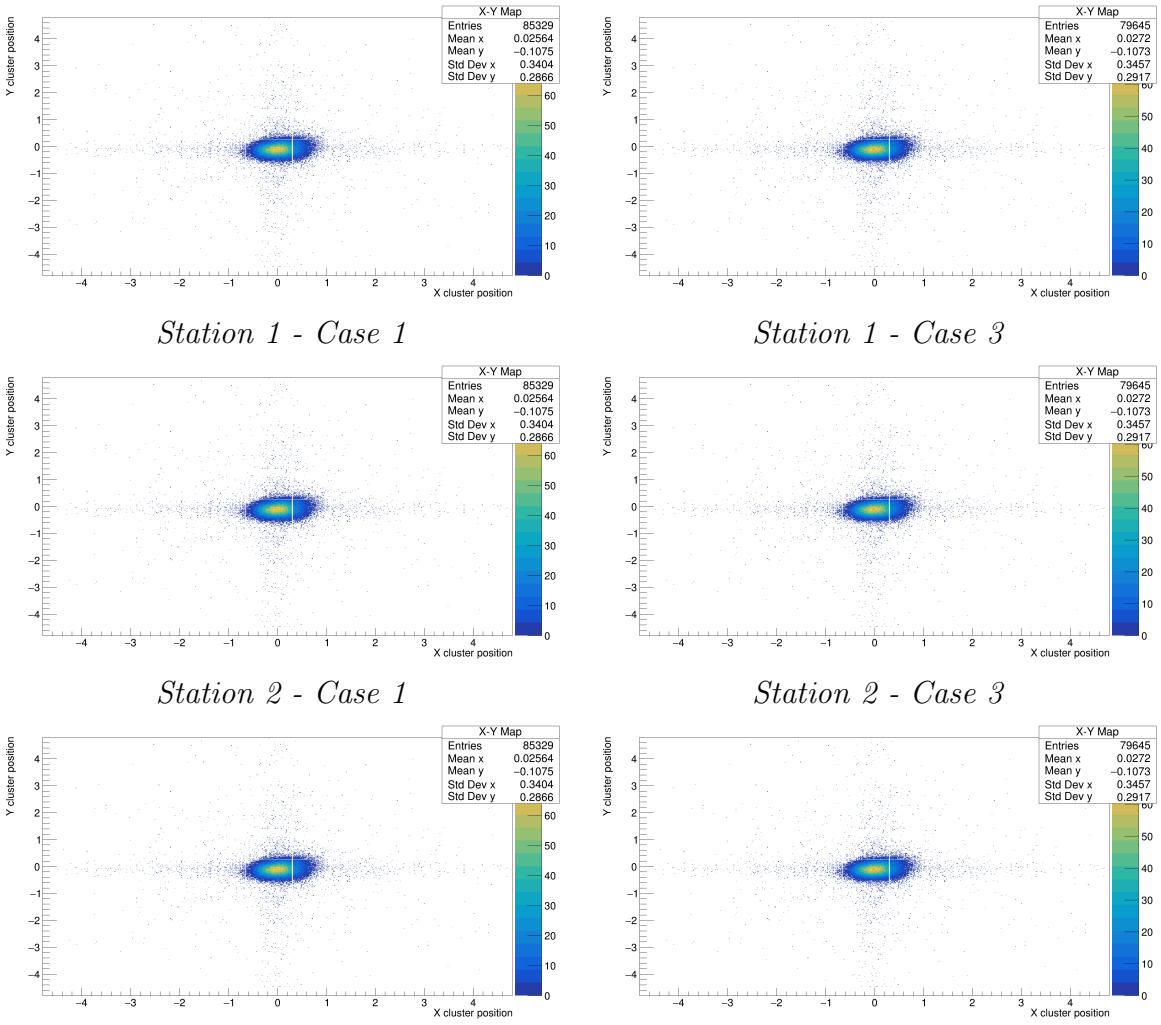

Station 1 - Case 1 *Station 1 - Case 3*

Station 2 - Case 1 *Station 2 - Case 3*

Station 3 - Case 1 *Station 3 - Case 3*

Figure 5.4: Cluster x-y map for the three station of MSD for *case 1* (left) and *case 3* (right).

5.2 η correction application

As explained in Section 4.4.2, correction values obtained by the correction map are applied, depending on η values, to the cluster signals.

5.2.1 GSI 2021

In Fig. 5.5 the signal dependence on η before the application of corrections is shown, presented for the six sensors of the MSD detector. The difference between intermediate region and reading region is evident: for $\eta \sim 1$ there is a value of $\sqrt{ADC}$ of 50, this value decreases up to 40 for $0.3 < \eta < 0.7$. Once the correction is applied, the dependence clearly changes as reported is Fig. 5.6. In this case, as expected, the behaviour is corrected thus signal values follows a straight line. Values around $\eta = 0$ and $\eta = 1$ remains a bit below the straight line. This is explained by the characteristic of the beam used in this data taking: ^{16}O beam at 400 MeV/u is over the limit of electronic saturation. In agreement with the effect described in 4.4.1. This fact is highlighted also by the cluster signal distribution difference before (Fig. 5.7) and after (Fig. 5.8) the correction.
The signal distribution is presented for all the sensor and for the total signal summing the contribution of all sensors (top histogram for both figures). In Fig. 5.7 there is a clear double peak shape of the signal describing the loss between two strips. While in the corrected case (Fig. 5.8), the distribution has one peak over the value of 50. However, this peak has a larger width respect to the uncorrected case suggesting the possibility to improve this correction.

5.2.2 CNAO 2022

The correction is applied also on two CNAO 2022 data run, for the purpose of checking the accuracy also on a different campaign.
Firstly the correction was analyzed for an alignment run (no target and no fragmentation processes) with a ^{12}C beam at 300 MeV/u which is characterized by a reduced number of events (10k).
In Fig. 5.9 the difference of the η function before and after the correction for sensors 3,4,5 and 6 are shown. The first two sensors are not taken in consideration due to some problems during the data taking. Another problem is the second line at low values of $\sqrt{ADC}$, noise due to problems in that run. Even if with a small number of events, the difference when the η correction is applied (bottom part of the figure) or not is visible: in this case, compared to GSI, the corrected cluster $\sqrt{ADC}$ has a flat behaviour respect to η also in readout regions ($\eta = 0$ and $\eta = 1$). There is no hint of saturation.

GSI2021

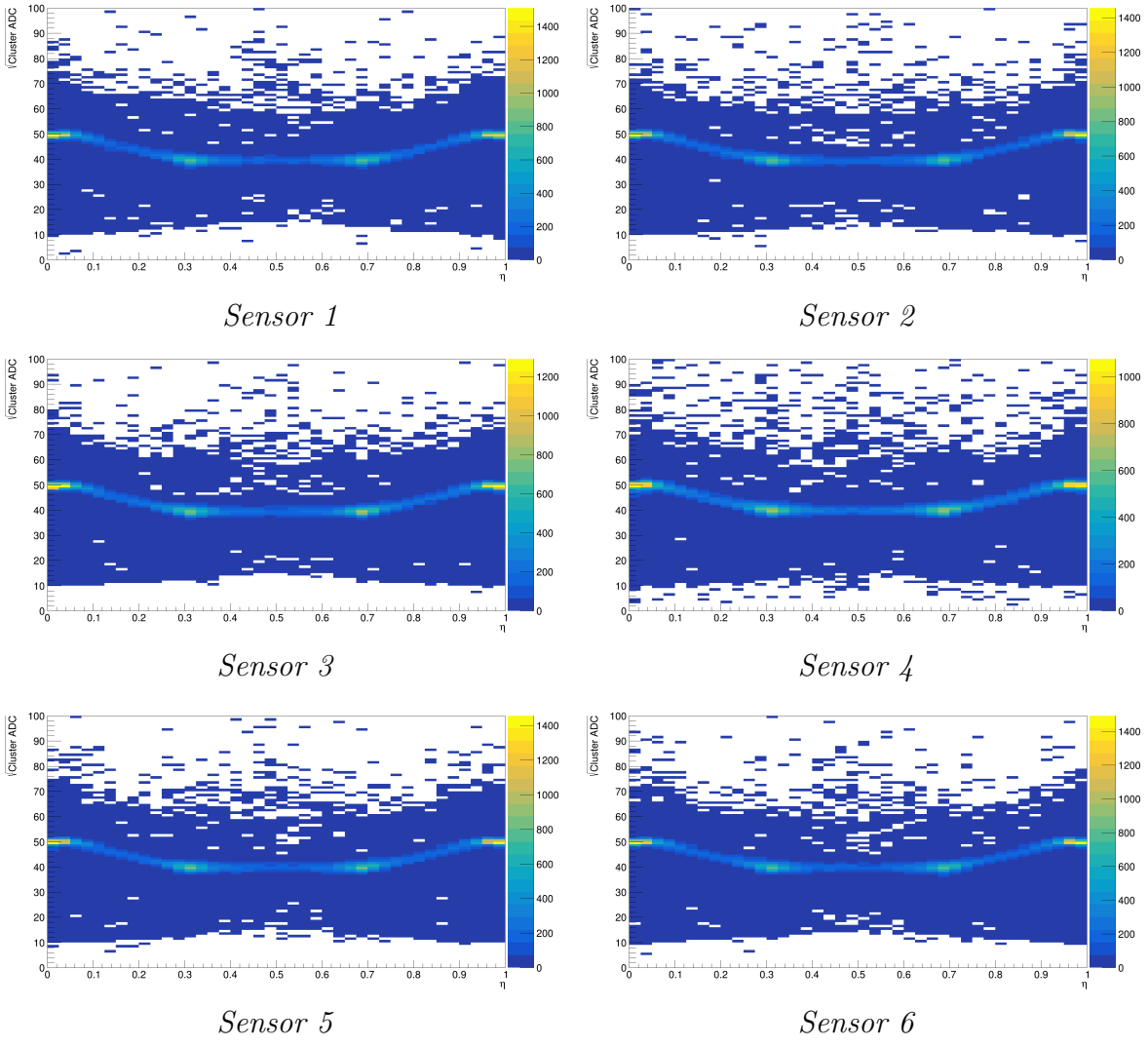

Sensor 1 *Sensor 2*

Sensor 3 *Sensor 4*

Sensor 5 *Sensor 6*

Figure 5.5: $\sqrt{ADC}$ in function of η for all six sensors. Sensor 1 and 2 (top), sensor 3 and 4 (center) and sensor 5 and 6 (bottom).

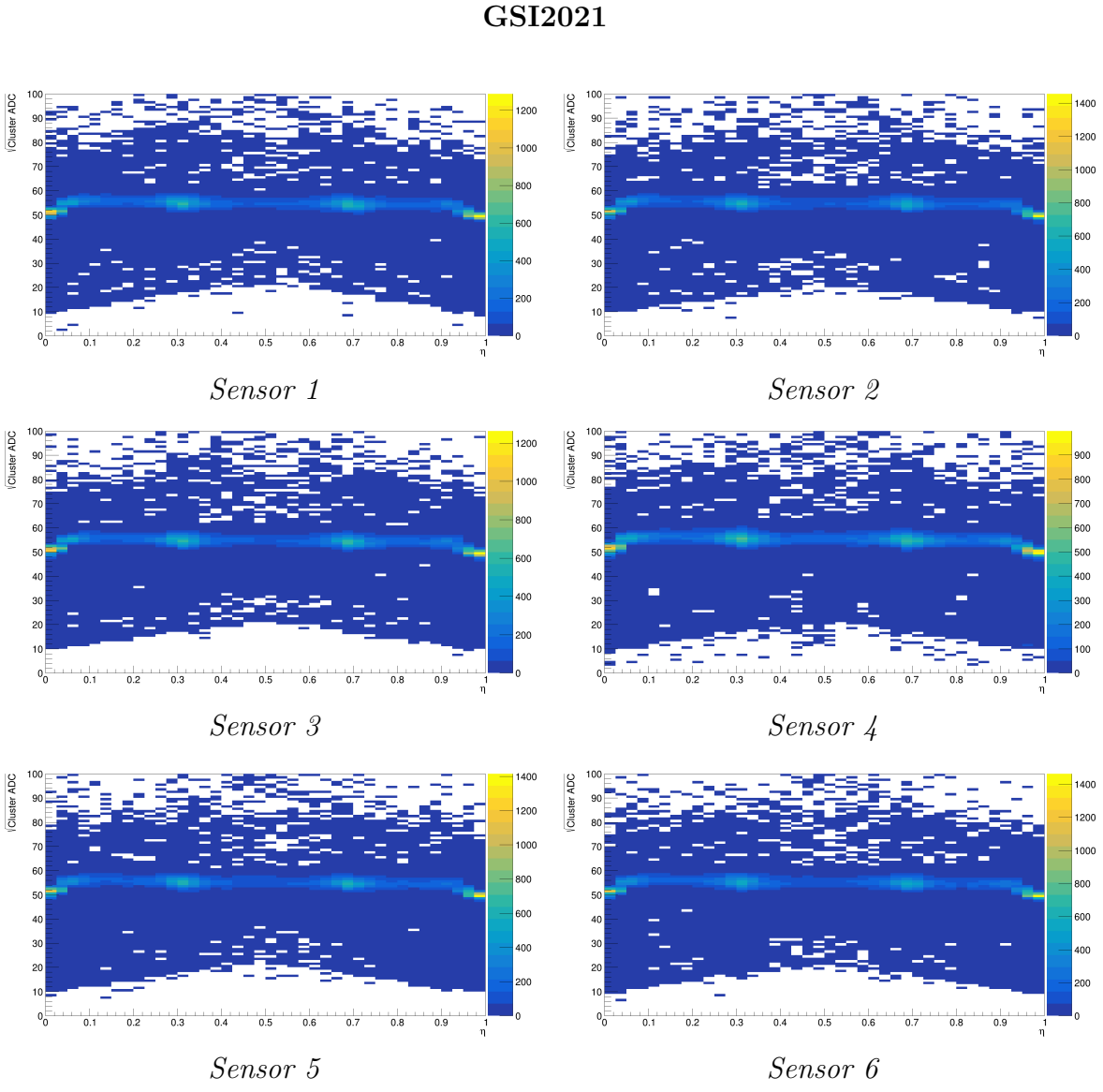

Figure 5.6: $\sqrt{ADC}$ in function of η for all six sensors after the correction. Sensor 1 and 2 (top), sensor 3 and 4 (center) and sensor 5 and 6 (bottom).

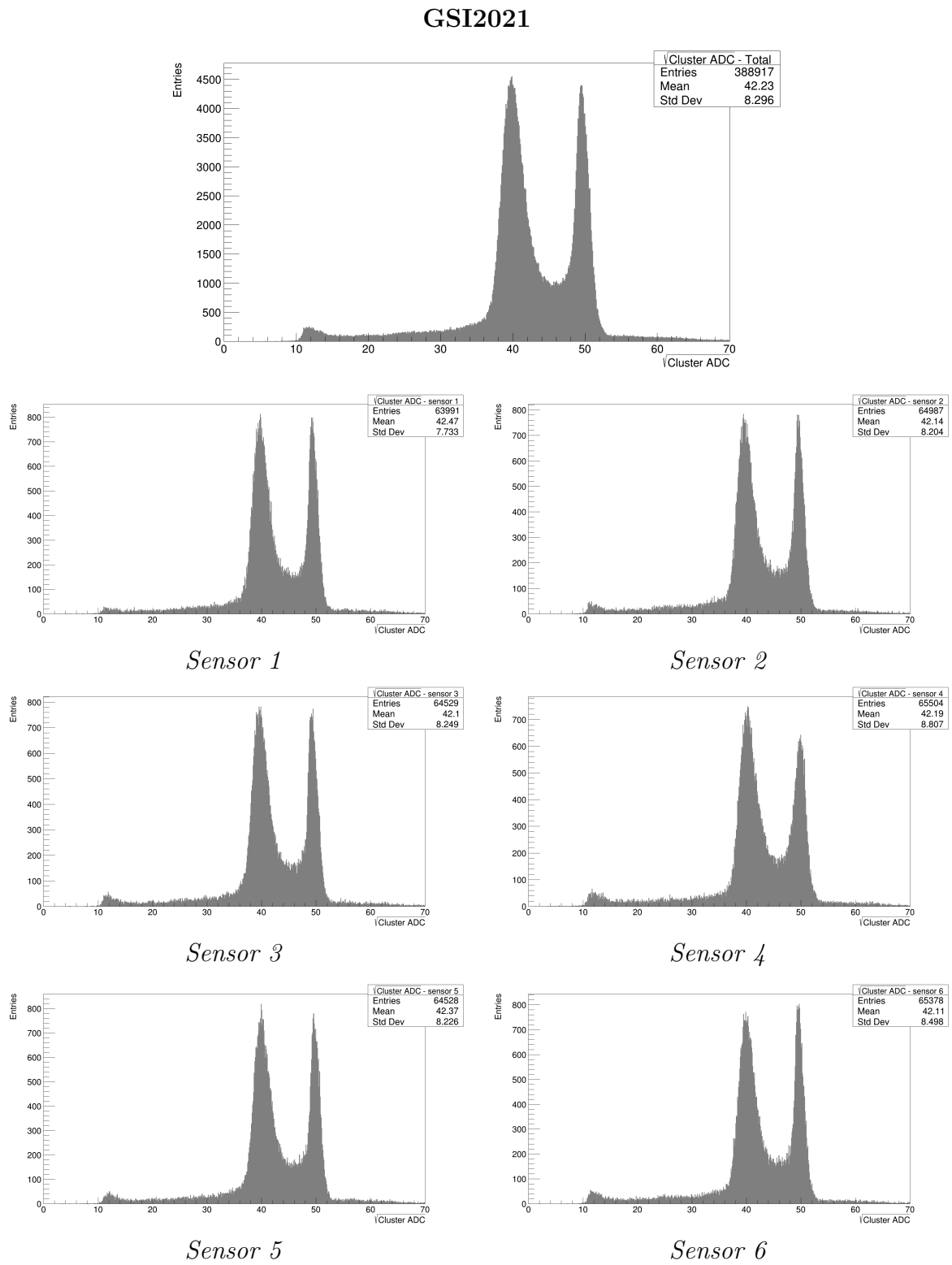

Figure 5.7: $\sqrt{ADC}$ before the η correction application. Total signal (above) and the six sensors in order (below).

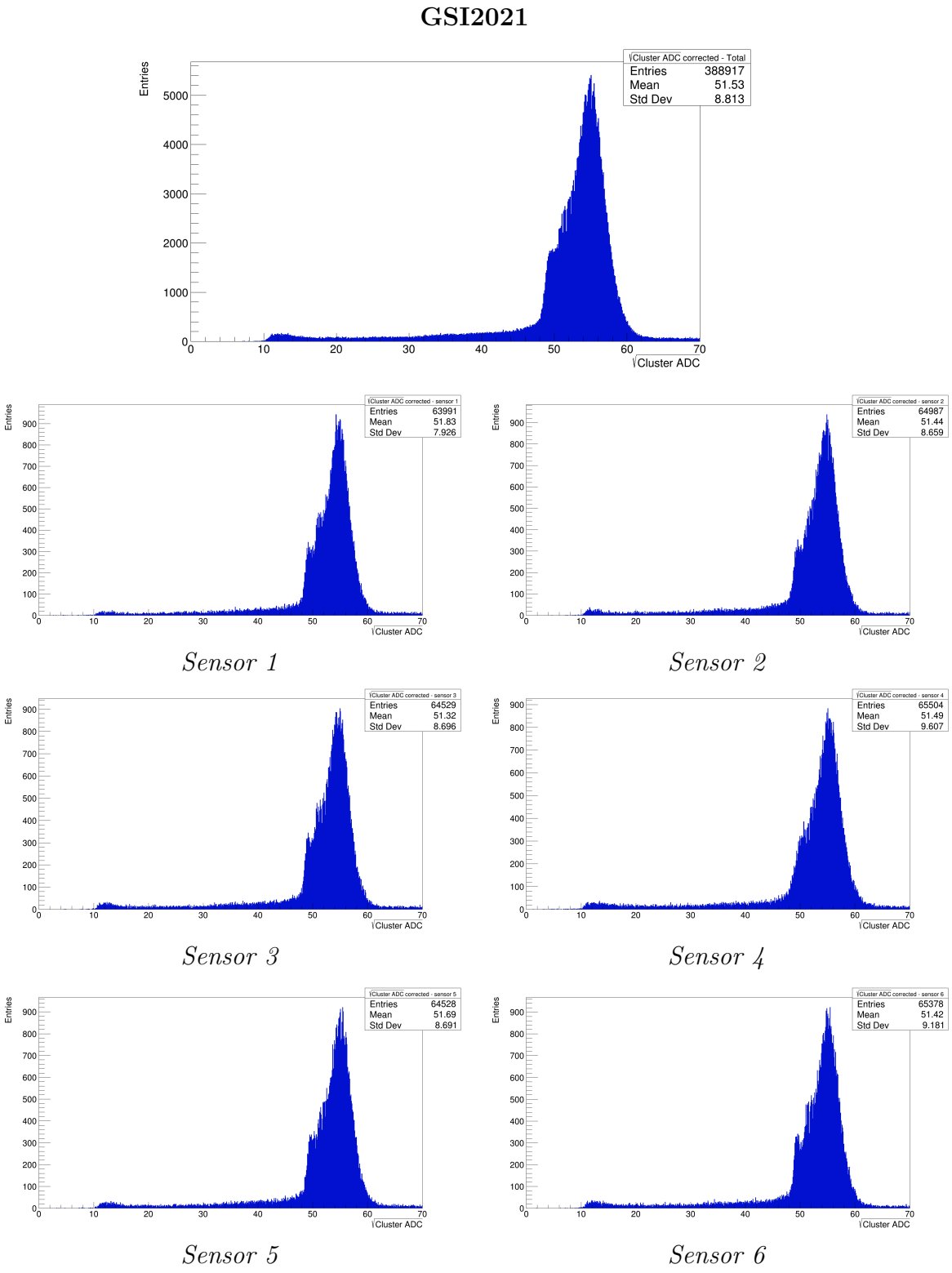

Figure 5.8: $\sqrt{ADC}$ after the η correction application. Total signal (above) and the six sensors in order (below).

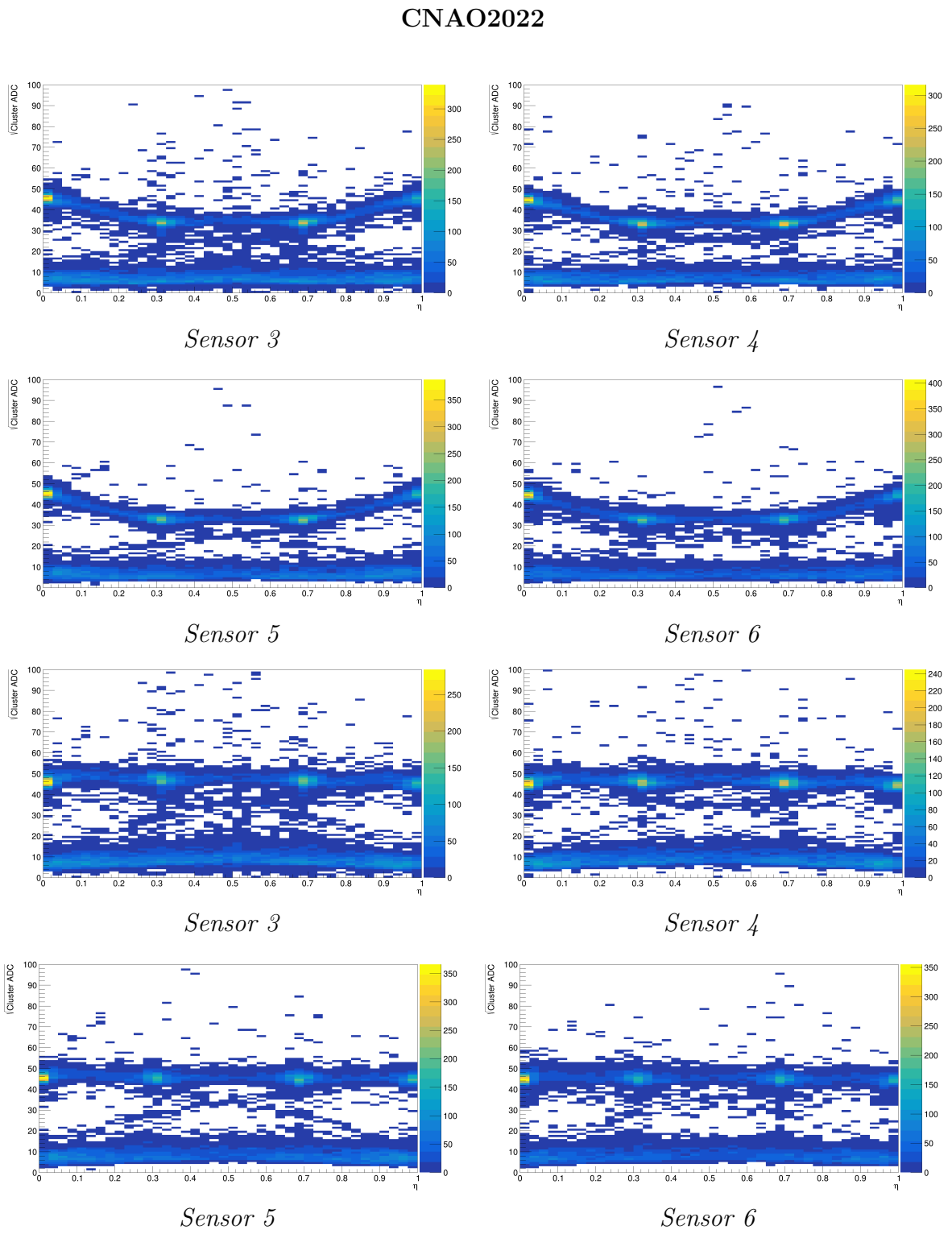

Figure 5.9: $\sqrt{ADC}$ in function of η for sensors 3,4,5 and 6: before (above) and after (below) the η correction.

In a second stage, the η correction was applied to a physics run characterized by a ^{12}C beam at 200 MeV/u and a carbon target of 5 mm. In this case there is another line for low values of $\sqrt{ADC}$ (from 0 to 10), this should be caused by a problem in noisy strip contribution which hides low z fragments produced in the interaction with target (Fig. 5.10).
The η correction produces an evident change in the behaviour of $\sqrt{ADC}$ (Fig. 5.11): the dependence is flat in η, but the signal has lower values for η around the readout regions ($\eta = 0$ and $\eta = 1$). The effect is similar to GSI 2021 case with Oxygen at 400 MeV/u described above. This is due to the fact that values of $\sqrt{ADC}$ are comparable between ^{12}C beam at 200 MeV/u and ^{12}O at 400 MeV/u. This is visible comparing the data of the two campaigns before (5.5 5.10) and after (5.6 5.11) the correction.

The correction applied is visible also in the the distribution of $\sqrt{ADC}$, shown for the total case and for all the sensors: the peaks shape is evident. The first peak in $\sqrt{ADC}$ between 0 and 10 is due to the problem in noise contribution. Then there are two peaks in $\sqrt{ADC}$ at 40 and 50 highlighting the signal loss in floating strips (Fig. 5.12). This is visible both for total signal and for all the sensors. After the correction application (Fig. 5.13), the two peaks merge into one with a values of almost 55. The change is pointed out also by the difference of the $\sqrt{ADC}$ mean value between before and after the application: it increases from 19.8 to 24.28. However, also the peak width is increased respect to uncorrected case, suggesting again that the η correction needs to be improved.

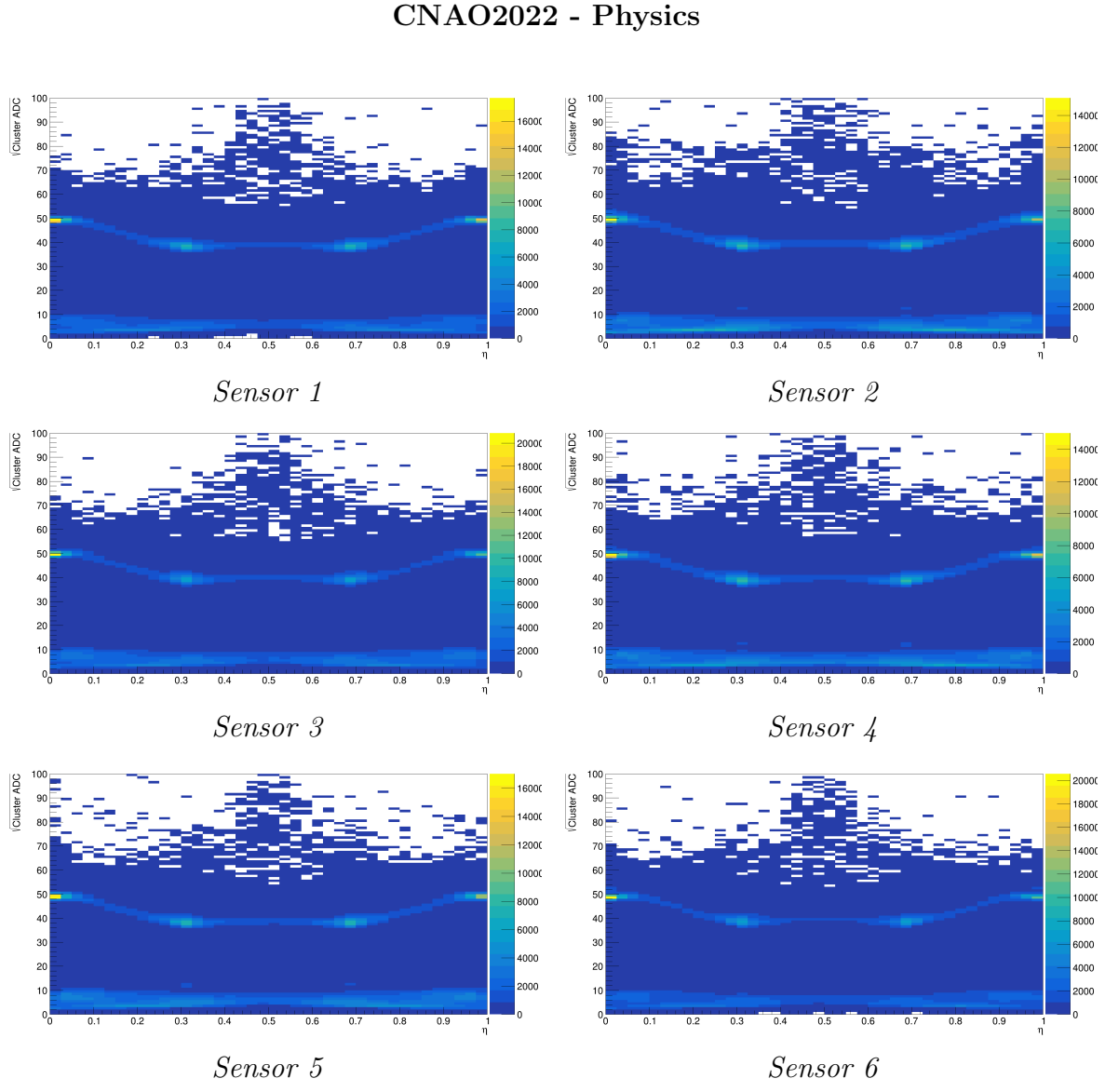

Figure 5.10: $\sqrt{ADC}$ in function of η for the six sensors of the MSD before the η correction.

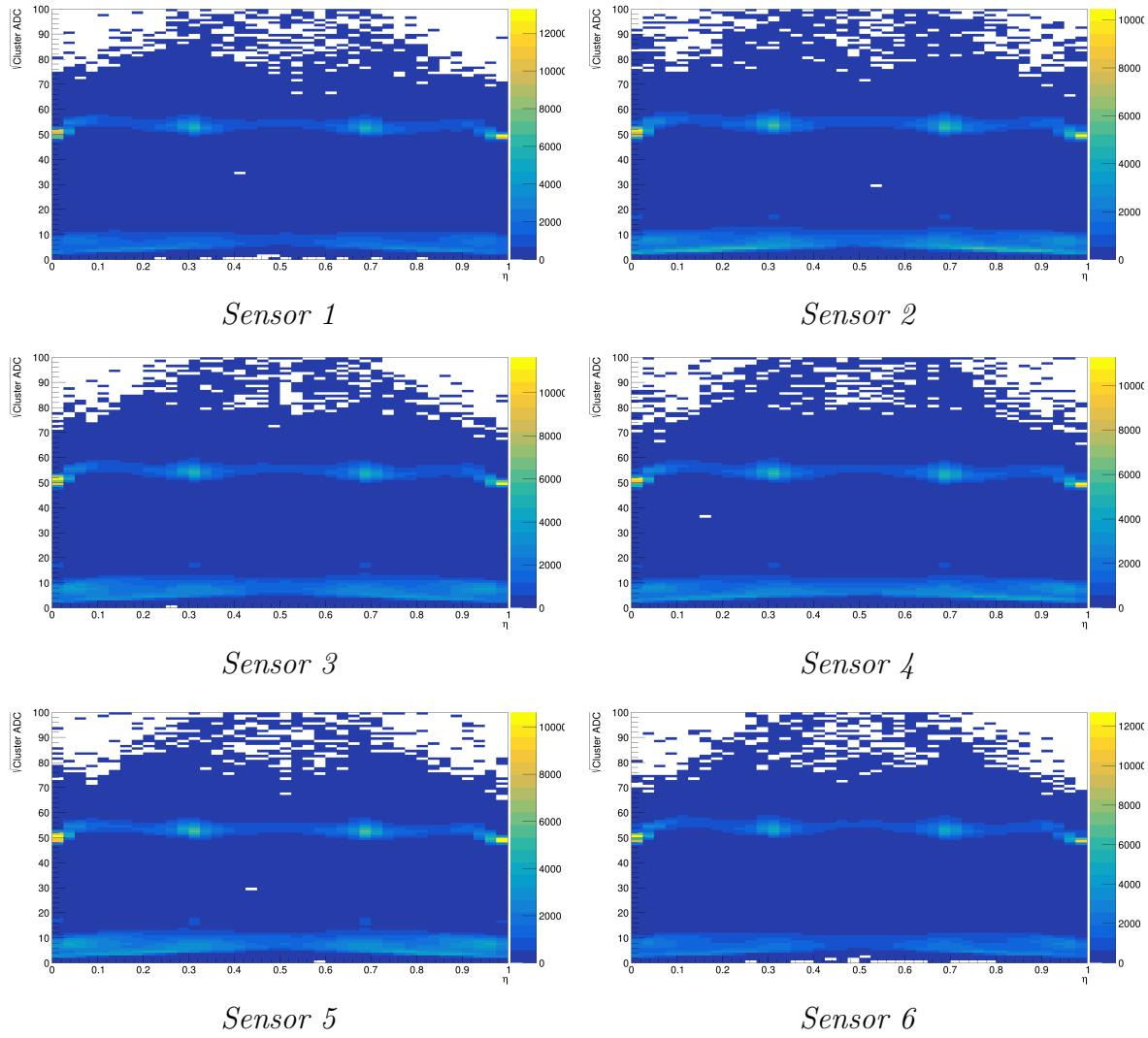

Figure 5.11: $\sqrt{ADC}$ in function of η for the six sensors of the MSD after the η correction.

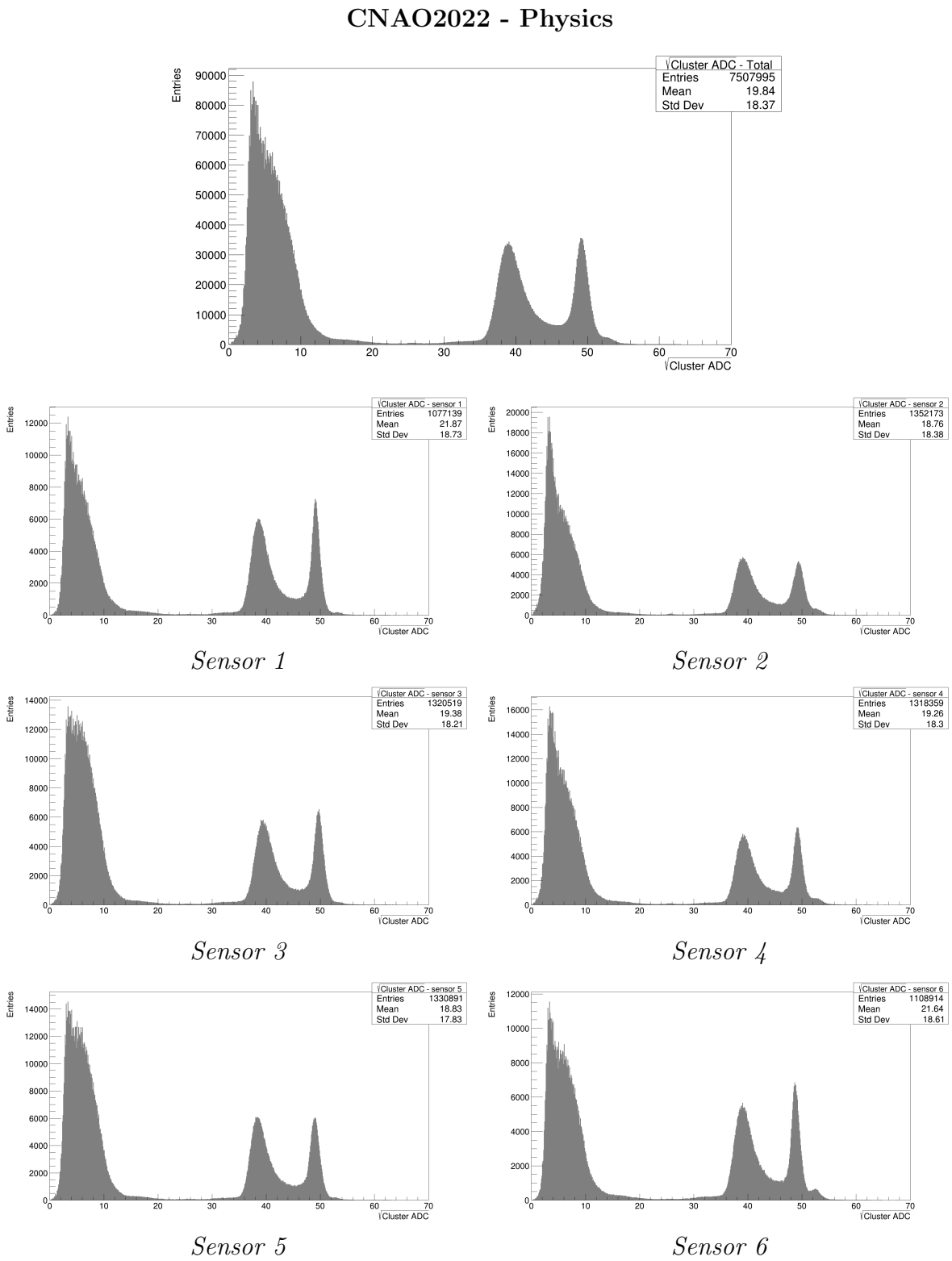

Figure 5.12: $\sqrt{ADC}$ before the η correction application. Total signal (above) and the six sensors in order (below).

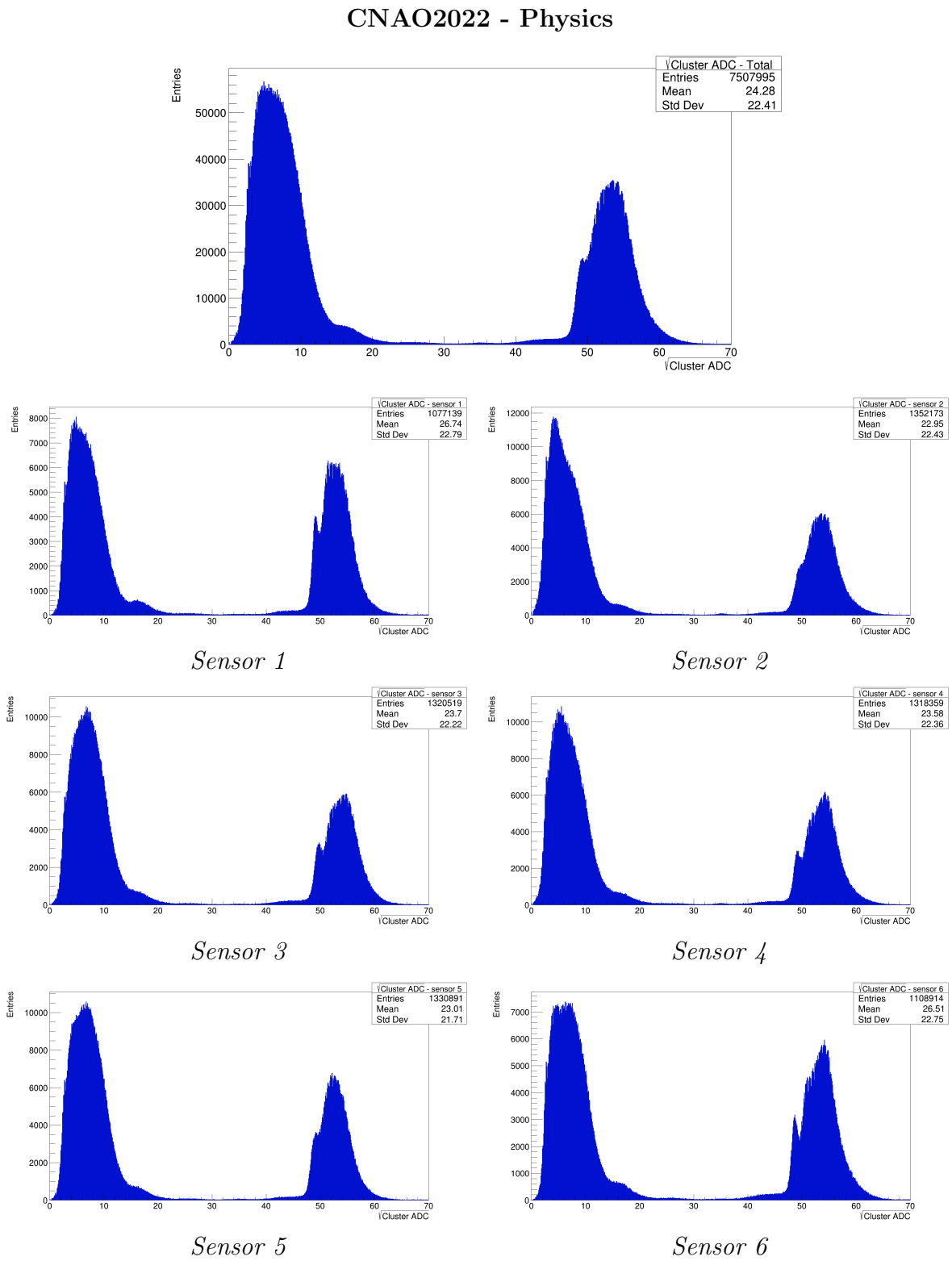

Figure 5.13: $\sqrt{ADC}$ after the η correction application. Total signal (above) and the six sensors in order (below).

Conclusions

In silicon microstrip detectors floating strips configuration is adopted in order to induce signal to the readout strips by means of capacitive coupling, improving the resolution with a smaller number of readout channels. However, previous results for charged ions interaction with silicon detector with this configuration have shown a charge loss for intermediate η region and non linear charge division between the strips. This effect is present also in the FOOT experiment MSD layout: signal for particles hitting near a floating strip is generally lower then the one for particles hitting near a readout strip. This signal division is influenced by the track's position with respect to the electrodes, the number of floating strips and their characteristics. The implementation proposed in this thesis handles this problem improving the clustering double threshold algorithm, analyzing data acquired at GSI and CNAO.

The first step on the analysis was to apply two improvements in the clustering algorithm: adding two strips at two extremes for all the clusters, in a way to exclude the possibility to have clusters with only one strips and an incorrect η definition. Then, also noisy strips are considered in the cluster composition. In this way clusters with noisy strips next to the seed are accepted, but in the end noisy strips are not considered in cluster properties computation. The new clusters configuration leads to an increase of two strips per cluster in size, with a change in position both for clusters and final points.

The second step starts with the corrections of cluster signals using gain factors: each VA chip of each sensor is corrected to equalize it to a reference value. Then the correction is applied in reference of the η value. Correction values were extracted from a map used in previous analysis for the HERD experiment (with the same sensors), to obtain a corrected ADC value of the cluster. The corrections are applied to the cluster $\sqrt{ADC}$, obtaining a flat distribution in η. In this way, also the energy loss value dE/dx is corrected, allowing a more precise measurement of the particle charge z from the Bethe-Bloch formula. For GSI 20121 data, the corrected signal values in the intermediate region are above the values in readout region. This is an artifact caused by the saturation of the electronics for heavy charged particles. The correction allows to have the correct flat distribution of the energy deposited. A slight lower value still remains in the sensor region ($\eta = 0$ and $\eta = 1$) due to the saturation of the detector electronics.

The same correction is then applied to CNAO 2022 data with ^{12}C at 200 and 300 MeV/u. For the alignment case at 300 MeV/u, characterized by a small number of events, an evident signal correction is obtained. Also in the physics case, where a carbon target of 5 mm was used, the η correction is visible, producing a signal behaviour similar to GSI 2021 situation. However the saturation influences again the correction due to the similar energy deposit of Carbon at 200 MeV/u and Oxygen at 400 MeV/u.

In conclusion, the improvements in the algorithm provide the expected change in clusters width and the η correction produces an evident increase of the signal. It allows to obtain an improved charge and energy resolution for the MSD impossible before the implementation of the η correction applied during this thesis work. However it needs to be improved checking also different physics cases, to do that a larger statistics is needed considering also different datasets for various campaign.
Further development of the clustering algorithm are needed to overcome the effects of electronics saturation, exploiting the info of the external strips of the cluster not used in the computation of the η parameter. All this results could give the possibility to improve also the charge resolution of the whole FOOT detector, helping future data taking and analysis.

Bibliography

[1] Particle Data Group et al. Review of particle physics. *Progress of Theoretical and Experimental Physics*, 2022(8):083C01, 2022.

[2] Particle data group PDG https://docs.google.com/viewer?url=http://pdg.lbl.gov/2006/reviews/passagerpp.pdf.

[3] Bruno Rossi. *High-energy particles*. NJ, 1952.

[4] William R Leo. *Techniques for nuclear and particle physics experiments: a how-to approach*. Springer Science & Business Media, 2012.

[5] H. A. Bethe. Molière's Theory of Multiple Scattering. *Phys. Rev.*, 89:1256–1266, Mar 1953.

[6] K Gunzert-Marx, H Iwase, D Schardt, and RS Simon. Secondary beam fragments produced by 200 mev u- 1 12c ions in water and their dose contributions in carbon ion radiotherapy. *New journal of physics*, 10(7):075003, 2008.

[7] Kenneth S Krane. *Introductory nuclear physics*. John Wiley & Sons, 1991.

[8] World Healt Organization. Health topics: Cancer https://www.who.int/health-topics/cancer.

[9] Facilities in operation: https://ptcog.site/index.php/facilities-in-operation-public.

[10] Fondazione CNAO: https://fondazionecnao.it/.

[11] Protonterapia Trento: https://protonterapia.provincia.tn.it/.

[12] CATANA Centro di AdroTerapia ed Applicazioni Nucleari Avanzate: https://www.lns.infn.it/it/applicazioni/catana.html.

[13] Sandro Rossi. Hadron Therapy Achievements and Challenges: The CNAO Experience. *Physics*, 4(1):229–257, 2022.

[14] Andrew E Ekpenyong. *Mathematical physics for nuclear experiments*. CRC Press, 2022.

[15] Daniele Davino. Theory, Design and Tests on a Prototype Module of a Compact Linear Accelerator for Hadrontherapy. 2002.

[16] Dirk Müssig. *Re-scanning in scanned ion beam therapy in the presence of organ motion*. PhD thesis, Technische Universitat Darmstadt, 2013.

[17] Philip Palin Dendy and Brian Heaton. *Physics for diagnostic radiology*. CRC press, 2011.

[18] Ute Linz. Physical and biological rationale for using ions in therapy. *Ion Beam Therapy: Fundamentals, Technology, Clinical Applications*, pages 45–59, 2011.

[19] Riccardo Ridolfi. Study of the track reconstruction in the FOOT experiment for Hadrontherapy, 2018.

[20] Marco Durante and Francis A. Cucinotta. Physical basis of radiation protection in space travel. *Rev. Mod. Phys.*, 83:1245–1281, Nov 2011.

[21] M. Tanabashi, K. Hagiwara, K. Hikasa, K. Nakamura, Y. Sumino, and et. al Takahashi. Review of particle physics. *Phys. Rev. D*, 98:030001, Aug 2018.

[22] W Li and MK Hudson. Earth's van allen radiation belts: From discovery to the van allen probes era. *Journal of Geophysical Research: Space Physics*, 124(11):8319–8351, 2019.

[23] John W Norbury, Jack Miller, Anne M Adamczyk, Lawrence H Heilbronn, Lawrence W Townsend, Steve R Blattnig, Ryan B Norman, Stephen B Guetersloh, and Cary J Zeitlin. Nuclear data for space radiation. *Radiation measurements*, 47(5):315–363, 2012.

[24] F Luoni, F Horst, CA Reidel, A Quarz, L Bagnale, L Sihver, U Weber, RB Norman, W De Wet, M Giraudo, et al. Total nuclear reaction cross-section database for radiation protection in space and heavy-ion therapy applications. *New Journal of Physics*, 23(10):101201, 2021.

[25] Fragmentation, Jul 2022. https://www.gsi.de/fragmentation.

[26] LW Townsend and JW Wilson. Energy-dependent parameterization of heavy-ion absorption cross sections. *Radiation research*, pages 283–287, 1986.

[27] Cary Zeitlin and Chiara La Tessa. The Role of Nuclear Fragmentation in Particle Therapy and Space Radiation Protection. *Frontiers in Oncology*, 6, 2016.

[28] Dataset Cross section https://www-nds.iaea.org/nrdc/basics/exfor-basics-1.html.

[29] Landolt-bornstein: https://materials.springer.com/bookshelf.

[30] J Dudouet, D Juliani, M Labalme, D Cussol, JC Angélique, B Braunn, J Colin, Ch Finck, JM Fontbonne, H Guérin, et al. Double-differential fragmentation cross-section measurements of 95 mev/nucleon 12 c beams on thin targets for hadron therapy. *Physical Review C*, 88(2):024606, 2013.

[31] G. Alexandrov, G. Battistoni, N. Belcari, S. t, M. u, G. Bruni, S. Brambilla, N. Camarlinghi, P. Cerello, E. Ciarrocchi, A. Clozza, G. Lellis, A. s, M. Durante, M. Emde, R. Faccini, V. Ferrero, F. Ferroni, C. Finck, and A. Zoccoli. FOOT CDR Conceptual Design, 08 2017.

[32] Giuliana Galati and Andrey Alexandrov et. al. Charge identification of fragments with the emulsion spectrometer of the FOOT experiment. *Open Physics*, 19(1):383–394, 2021.

[33] Giuseppe Battistoni, Marco Toppi, Vincenzo Patera, and The Collaboration. Measuring the Impact of Nuclear Interaction in Particle Therapy and in Radio Protection in Space: the FOOT Experiment. *Frontiers in Physics*, 8, 02 2021.

[34] GSI facility: https://www.gsi.de/en/researchaccelerators/accelerator-facility.

[35] FOOT TWiki http://arpg-serv.ing2.uniroma1.it/twiki/bin/view/main/footsoftware.

[36] Rene Brun and Fons Rademakers. ROOT-An object oriented data analysis framework. *Nuclear instruments and methods in physics research section A: accelerators, spectrometers, detectors and associated equipment*, 389(1-2):81–86, 1997.

[37] SHOE repository. https://baltig.infn.it/asarti/shoe, 2023.

[38] Giuseppe Battistoni, Julia Bauer, Till T Boehlen, Francesco Cerutti, Mary PW Chin, Ricardo Dos Santos Augusto, Alfredo Ferrari, Pablo G Ortega, Wioletta Kozłowska, Giuseppe Magro, et al. The FLUKA code: an accurate simulation tool for particle therapy. *Frontiers in oncology*, 6:116, 2016.

[39] Gamma Medica-Ideas, VA140 Document Datasheet (V0R1).

[40] K. Kanxheri, M. Barbanera, G. Ambrosi, G. Silvestre, S. Biondi, R. Ridolfi, M. Villa, D. Aisa, M. Caprai, M. Ionica, P. Placidi, L. Servoli, and on behalf of the FOOT collaboration. The Microstrip Silicon Detector (MSD) data acquisition system architecture for the FOOT experiment. *Journal of Instrumentation*, 17(03):C03035, mar 2022.

[41] Wojciech Kucewicz and Maciej Pilch. Low noise silicon microstrip detector. *Nuclear Physics B-Proceedings Supplements*, 61(3):330–334, 1998.

[42] Andrey Alexandrov, Behcet Alpat, Giovanni Ambrosi, Stefano Argirò, Diaz Raul Arteche, Mattia Barbanera, Nazar Bartosik, Giuseppe Battistoni, Nicola Belcari, Elettra Bellinzona, et al. Characterization of 150 μm thick silicon microstrip prototype for the foot experiment. *Journal of Instrumentation*, 17(12):P12012, 2022.

[43] Gianluigi Silvestre. Development of the external tracker of the FOOT experiment, PHD Thesis, 2021.

[44] D Lietti, A Berra, M Prest, and E Vallazza. A microstrip silicon telescope for high performance particle tracking. *Nuclear Instruments and Methods in Physics Research Section A: Accelerators, Spectrometers, Detectors and Associated Equipment*, 729:527–536, 2013.

[45] C Altomare, G Ambrosi, M Barbanera, B Bertucci, YX Cui, M Duranti, V Formato, K Gong, M Graziani, JH Guo, et al. The Silicon Charge Detector of the High Energy Cosmic Radiation Detection facility. 2023.